Monthly Notices
of the
ROYAL ASTRONOMICAL SOCIETY

Mon. Not. R. Astron. Soc. **427,** 127–145 (2012) doi:10.1111/j.1365-2966.2012.21948.x

PARSEC: stellar tracks and isochrones with the PAdova and TRieste Stellar Evolution Code

Alessandro Bressan,[1⋆] Paola Marigo,[2] Léo Girardi,[3] Bernardo Salasnich,[3] Claudia Dal Cero,[4] Stefano Rubele[3] and Ambra Nanni[1]

[1]*SISSA, via Bonomea 265, I-34136 Trieste, Italy*
[2]*Dipartimento di Fisica e Astronomia Galileo Galilei, Università di Padova, Vicolo dell'Osservatorio 3, I-35122 Padova, Italy*
[3]*Osservatorio Astronomico di Padova, Vicolo dell'Osservatorio 5, I-35122 Padova, Italy*
[4]*Liceo Scientifico Paritario Gymnasium Patavinum Sport, via P.G.Guarneri 22, I-35132 Padova, Italy*

Accepted 2012 August 16. Received 2012 August 15; in original form 2012 April 10

ABSTRACT

We present the updated version of the code used to compute stellar evolutionary tracks in Padova. It is the result of a thorough revision of the major input physics, together with the inclusion of the pre-main sequence phase, not present in our previous releases of stellar models. Another innovative aspect is the possibility of promptly generating accurate opacity tables fully consistent with *any* selected initial chemical composition, by coupling the Opacity Project At Livermore (OPAL) data at high temperatures to the molecular opacities computed with our ÆSOPUS code. In this work, we present extended sets of stellar evolutionary models for various initial chemical compositions, while other sets with different metallicities and/or different distributions of heavy elements are being computed. For the present release of models, we adopt the solar distribution of heavy elements from the recent revision by Caffau et al., corresponding to a Sun's metallicity $Z \simeq 0.0152$. From all computed sets of stellar tracks, we also derive isochrones in several photometric systems. The aim is to provide the community with the basic tools to model star clusters and galaxies by means of population synthesis techniques.

Key words: stars: evolution – Hertzsprung–Russell and colour magnitude diagrams – stars: interiors – stars: low-mass.

1 INTRODUCTION

In this paper, we briefly describe our new stellar evolution code PARSEC: the PAdova and TRieste Stellar Evolution Code. This is the result of a thorough revision and update of the stellar evolution code used in Padova to compute sets of stellar evolutionary tracks that are widely used by the astronomical community (Bressan et al. 1993; Bertelli et al. 1994, 2008, 2009; Girardi et al. 2000; Marigo et al. 2001).

As we describe next, the most important changes include the updating of the major input physics (equation of state, opacities, nuclear reaction rates), the implementation of microscopic diffusion and the extension of the evolutionary calculations to the pre-main sequence (PMS) phase.

We have devoted much care to ensure consistency between the adopted chemical mixture and the physical ingredients in PARSEC, i.e. opacities and equation of state (EOS), as detailed in Sections 2.2 and 2.3, respectively. In this respect, a distinctive prerogative of our stellar models is the use of the ÆSOPUS tool (Marigo & Aringer 2009) that enables us to compute tables of accurate low-T opacities for *any* specified mixture of chemical elements from H to U, just starting from the monochromatic absorption coefficients of all opacity sources under consideration (e.g. line lists of several molecules). We have put the most possible effort to keep the same abundance flexibility also when dealing with the EOS, the high-temperature radiative opacities and the conductive opacities for which we have employed other public codes. This represents a key aspect since we are now able to predict readily the evolution of stars for any chemical pattern of interest (varying CNO abundances, different degrees of enhancement/reduction in α elements, C–N, Ne–O and Mg–Al abundance anti-correlations suitable for Galactic globular clusters, etc.).

In this paper, we present new sets of evolutionary tracks for the initial chemical compositions in the range from $Z = 0.0005$ to 0.07. The helium content Y is assumed to increase with Z. Other metallicities and arbitrary distributions of heavy elements are being considered. The range of initial masses is from 0.1 to 12 $M_\odot$,

⋆E-mail: alessandro.bressan@sissa.it

Table 1. Solar abundances of a few elements adopted in this work, following the values recommended by Caffau et al. (2011) and references therein. Abundances are expressed with the standard notation $A(Y) = \log(n_Y/n_H) + 12$. For all other species, we adopt the compilation of Grevesse & Sauval (1998).

Element	Abundance $A(Y)$	Reference
Li	1.03	Caffau et al. (2011)
C	8.50	Caffau et al. (2010)
N	7.86	Caffau et al. (2009)
O	8.76	Caffau et al. (2008)
P	5.46	Caffau et al. (2007)
S	7.16	Caffau & Ludwig (2007)
K	5.11	Caffau et al. (2011)
Fe	7.52	Caffau et al. (2011)
Eu	0.52	Mucciarelli et al. (2008)
Hf	0.87	Caffau et al. (2008)
Os	1.36	Caffau et al. (2011)
Th	0.08	Caffau et al. (2008)

and the evolutionary phases extend from the PMS till either the onset thermally pulsing asymptotic giant branch (TP-AGB) phase or carbon ignition. From all these tracks, we also derive isochrones in several photometric systems.

The plan of this paper is as follows. Section 2 presents the input physics of the models which includes the new solar distribution of elements. Section 3 deals with the calibration of important model parameters with the Solar model. Section 4 briefly describes other adopted element distributions and global metallicities. Section 5 introduces the new stellar tracks and discusses their main characteristics and Section 6 describes the corresponding isochrones.

2 INPUT PHYSICS

2.1 The solar distribution of heavy elements

Before discussing any other relevant input physics, we specify the *solar* distribution of heavy elements adopted in this paper. For each element heavier than ^{4}He, we must assign its fractional abundance relative to the total solar metallicity, i.e. $X_{i,\odot}/Z_\odot$. This will be the reference distribution, with respect to which other *non-scaled solar* mixtures will be considered.

The reference solar distribution of metals consists of 90 chemical elements[1] from Li to U, with abundances taken from the compilation by Grevesse & Sauval (1998), except for a subset of species for which we adopt the recommended values according to the latest revision by Caffau et al. (2011) and references therein. The solar abundances of the recently revised elements are listed in Table 1.[2]

According to this abundance compilation, the present-day Sun's metallicity is $Z_\odot = 0.015\,24$ that can be compared to other recent estimates, e.g. $Z_\odot = 0.0141$ of Lodders, Palme & Gail (2009) and $Z_\odot = 0.0134$ of Asplund et al. (2009).

In addition to the solar one, other chemical distributions have been considered in this work, which should be representative of galaxies with specific chemical evolution histories such as, for instance, the Magellanic Clouds, massive early-type galaxies or other systems with α-enhanced or α-depleted patterns.

2.2 Opacities

Following a standard procedure, in PARSEC we describe the absorption properties of matter in the gas phase by means of pre-computed, static tables of Rosseland mean opacities, $\kappa_R(\rho, T)$, which are suitably arranged to encompass a region of the temperature–density ($T-\rho$) plane wide enough to cover all values met across the stellar structure during the evolution.[3]

Besides the state variables, T and ρ, opacities depend on the chemical composition of the gas, which is commonly specified by a set of abundance parameters, i.e. the total metallicity Z, the hydrogen abundance X and the distributions $\{X_i/Z\}$ of the heavy elements in the mixture. The latter depend on the specific case under consideration, e.g. scaled-solar mixtures with $\{X_i/Z\} = \{X_i/Z\}_\odot$ or others $\{X_i/Z\}$ derived from various constraints such as the enhancement/depletion of α elements (expressed by the ratio [α/Fe]) or the over-abundances in primary C and O necessary to describe the He-burning regions. For the computation of the opacity tables, we employ different programmes as detailed below.

In the high-temperature regime, $4.2 \leq \log(T/\mathrm{K}) \leq 8.7$, we adopt the opacity tables provided by the Opacity Project At Livermore (OPAL) team (Iglesias & Rogers 1996, and references therein). We use the OPAL interactive web mask[4] specifying the number fractions of 19 heavy elements (C, N, O, Ne, Na, Mg, Al, Si, P, S, Cl, Ar, K, Ca, Ti, Cr, Mn, Fe and Ni), as implied by our set of X_i/Z.

In the low-temperature regime, $3.2 \leq \log(T/\mathrm{K}) \leq 4.1$, we employ the ÆSOPUS[5] tool (Marigo & Aringer 2009) to generate opacity tables for any specified set of chemical abundances for 92 elements from H to U. ÆSOPUS solves the EOS of matter in the gas phase for ≈800 chemical species consisting of almost 300 atoms (neutral atoms and ions up to fifth ionization stage) and 500 molecular species. The gas opacities account for many continuum and discrete sources, including atomic opacities, molecular absorption and collision-induced absorption.

In the transition interval $4.0 < \log(T/\mathrm{K}) < 4.1$, a linear interpolation between the opacities derived from the OPAL and ÆSOPUS is adopted. We remind the reader that both opacities sources provide values in good agreement in this temperature interval. As shown by Marigo & Aringer (2009, see their fig. 7) the logarithmic differences between OPAL and ÆSOPUS opacities are lower than 0.05 dex for most cases.

Conductive opacities are included following Itoh et al. (2008). In the computation, for any specified chemical mixture, the total thermal conductivity accounts for the contribution of 11 atomic species (^{1}H, ^{4}He, ^{12}C, ^{14}N, ^{16}O, ^{20}Ne, ^{24}Mg, ^{28}Si, ^{32}S, ^{40}Ca and ^{56}Fe), each weighted by the corresponding abundance (by number). To this aim, we have implemented in our code the FORTRAN routine kindly made available by Itoh (private communication).

[1] A few elements (Po, At, Rn, Fr, Ra, Ac and Pa) are assigned negligible abundances.

[2] Some of the elements listed in Table 1 (e.g. Eu, Hf, Th) may be irrelevant for the evolutionary calculations presented in this paper; however, they will become relevant in the context of the TP-AGB tracks, to be described in subsequent papers.

[3] Under the assumption of local thermodynamical equilibrium and in the limit of diffusion approximation, the solution of the radiation transfer equation simplifies in such a way that the flux of radiation F as a function of radius r is expressed as $F(r) \propto 1/\kappa_R$.

[4] http://opalopacity.llnl.gov/

[5] http://stev.oapd.inaf.it/aesopus

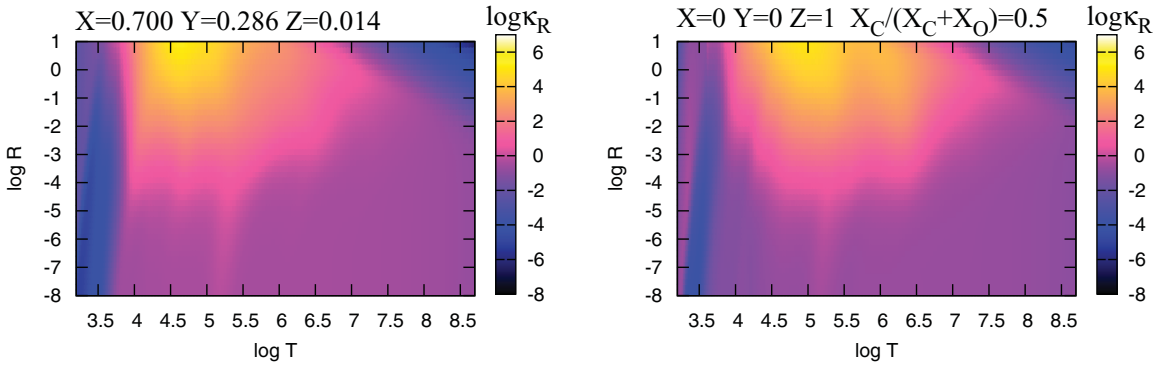

Figure 1. Maps of Rosseland mean opacities showing the actual coverage of the tables in the $\log(T) - \log(R)$ plane. While both plots refer to the same reference metallicity $Z = 0.014$, the left-hand panel exemplifies the case of an 'H-rich' table, and the right-hand panel corresponds to an 'H-free' table, suitable to describe the opacity of a gas in which all helium has been burnt and converted into carbon and oxygen in the same proportions.

In practice, given the total reference metallicity Z and the distribution of heavy elements $\{X_i/Z\}$, we construct two sets of opacity tables, to which we simply refer to as 'H-rich' and 'H-free' opacities. The former set comprises N_X opacity tables, where N_X denotes the number (typically 10) of hydrogen abundance values, ranging from $X = 0$ to $1 - Z$. The latter set is characterized by $X = 0$, while the helium content assumes N_Y values (typically $N_Y = 10$), ranging from $Y = 0$ to $1 - Z$. In addition, for each Y value, we consider three combinations of C and O abundances, defined by the ratios $R_C = X_C/(X_C + X_O) = 0.0, 0.5, 1.0$. All other elements are left unchanged. The 'H-free' tables are specifically designed to describe the opacity in the He-burning regions.

For both sets, each opacity table covers a rectangular region defined by the intervals $3.2 \leq \log(T/\mathrm{K}) \leq 8.7$ and $-8 \leq \log(R) \leq 1$, where $R = \rho/T_6$ in g cm^{-3} and $T_6 = T/(10^6\ \mathrm{K})$. To limit as much as possible the accuracy loss due to subsequent interpolation, we adopt a fine grid spacing, with $\Delta \log T = 0.01$ for $3.2 \leq \log(T/\mathrm{K}) < 3.7$, $\Delta \log T = 0.02$ for $3.7 \leq \log(T/\mathrm{K}) \leq 8.7$, and $\Delta \log R = 0.2$. Two examples of opacity tables for both the 'H-rich' and 'H-free' cases are given in Fig. 1. The maps are obtained with the same grid spacing of the tables, which actually provides quite a dense and smooth description of the opacity all over the thermodynamic domain of interest.

Interpolation over 'H-rich' tables is performed in four dimensions, i.e. using R, T, X and Z as the independent variables. While the interpolation in R and T is bilinear, we adopt a parabolic scheme for both X and Z interpolation. Interpolation over 'H-free' tables is performed in five dimensions, i.e. involving R, T, Y, $R_C = X_C/(X_C + X_O)$ and Z. Interpolation is bilinear in R and T, linear in R_C, while we use as before a parabolic scheme for Z interpolation.

Actually, bilinear interpolation in R and T does not preserve the continuity of the first derivatives, possibly introducing some instability into the convergence of the stellar model. For this reason, once the opacity tables are loaded, we compute and store the logarithmic derivatives of the opacities (with respect to T and R) over the same grid of the opacity tables. Hence, the partial derivatives can be obtained by bilinear interpolation, in the same way as for the opacity values. While fulfilling the continuity requirements of the derivatives, this method also has the advantage of being quite fast. It should also be specified that, for each planned set of stellar tracks, the PARSEC code preliminarily loads a suitable number N_Z of opacity tables in order to follow in detail any significant change in the local metal content Z due, for instance, to the diffusion of heavy elements or dredge-up episodes.

2.3 Equation of state

For the EOS, we make use of the FREEEOS code developed and updated over the years by Irwin, and freely available under the GNU General Public License.[6] The FREEEOS package is fully implemented in our code and we may use it 'on-the-fly', for different approximations and levels of accuracy. However, since the pre-tabulated version is sufficiently accurate for most of our purposes, we proceed by pre-computing suitable tables and by interpolating between them.

The EOS calculation is performed accounting for the contributions of several elements, namely H, He, C, N, O, Ne, Na, Mg, Al, Si, P, S, Cl, Ar, Ca, Ti, Cr, Mn, Fe and Ni. For any specified distribution of heavy elements $\{X_i/Z\}$, we consider several values of the metallicity Z, and for each value of Z we pre-compute tables containing all thermodynamic quantities of interest (e.g. mass density, mean molecular weight, entropy, specific heats and their derivatives, etc.) over suitably wide ranges of temperature and pressure. Exactly in the same fashion as for the opacity, we arrange an 'H-rich' set containing $N_X = 10$ tables each characterized by different H abundances, and an 'H-free' set consisting of 31 tables, which are designed to describe He-burning regions. In practice we consider 10 values of the helium abundance, from $Y = 0$ to $1 - Z$. For each Y, we compute three tables with C and O abundances determined by the ratios $R_C = X_C/(X_C + X_O) = 0.0, 0.5, 1.0$.

Multi-dimension interpolations (in the variables Z, X or Y and R_C) are carried out with the same scheme adopted for the opacities. All interesting derivatives are pre-computed and included in the EOS tables.

Our procedure is to minimize the effects of interpolation by computing a set of EOS tables exactly with the initial metallicity and partition of the new set of tracks. This set is then inserted into the EOS data base for interpolation when the global metallicity Z changes during the evolution.

Before proceeding with the calculation of evolutionary tracks, we extensively tested the accuracy of the interpolation method. Fig. 2 illustrates the typical results from these tests: it compares evolutionary tracks computed with either the interpolation within the tabulated EOS or a direct call to FREEEOS for each mesh point. As can be appreciated, the differences in the Hertzsprung–Russell (HR) diagram are clearly negligible. The same applies to other quantities in the tracks, such as the lifetimes and the luminosity at the RGB tip.

[6] http://freeeos.sourceforge.net/

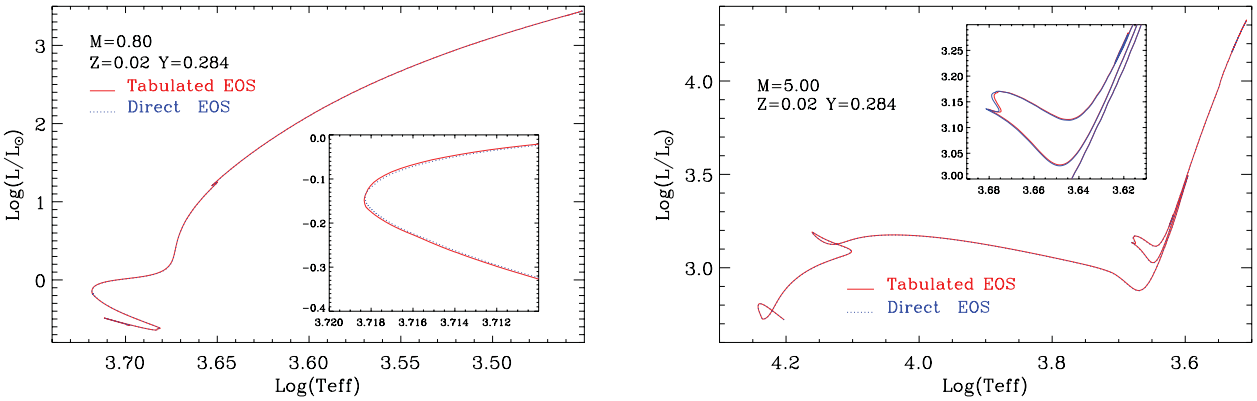

Figure 2. Comparison between evolutionary tracks computed with the direct calculation of FREEEOS, or interpolating between pre-tabulated FREEEOS tables. The differences between these two cases are clearly negligible.

2.4 Nuclear reaction rates

Our nuclear network consists of the p–p chains, the CNO tri-cycle, the Ne–Na and Mg–Al chains, and the most important α-capture reactions, including the α–n reactions. The network solves for the abundances of $N_{\rm el} = 26$ chemical species: ^{1}H, D, ^{3}He, ^{4}He,^{7}Li, ^{8}Be, ^{4}He, ^{12}C, ^{13}C, ^{14}N, ^{15}N, ^{16}N, ^{17}N, ^{18}O, ^{19}F, ^{20}Ne, ^{21}Ne, ^{22}Ne, ^{23}Na, ^{24}Mg, ^{25}Mg, ^{26}Mg, ^{26}Al^{m}, ^{26}Al^{g}, ^{27}Al, ^{28}Si. The latter nucleus acts as the 'exit element', which terminates the network. In total, we consider 42 reaction rates, listed in Table 2. These are the recommended rates in the JINA REACLIB data base (Cyburt et al. 2010) from which we also take the Q value of each reaction.

The electron screening factors for all reactions are those from Dewitt et al. (1973) and Graboske et al. (1973). The abundances of the various elements are evaluated with the aid of a semi-implicit extrapolation scheme, as described in Marigo et al. (2001). This technique, which does not assume nuclear equilibrium, is a convenient compromise between the higher accuracy typical of the explicit scheme, and the better stability of the solution guaranteed by the implicit scheme.

2.5 Neutrino losses

Energy losses by electron neutrinos are taken from Munakata, Kohyama & Itoh (1985) and Itoh & Kohyama (1983), but for plasma neutrinos, for which we use the fitting formulae provided by Haft, Raffelt & Weiss (1994).

2.6 Convection

2.6.1 Overshoot from the convective core

The extension of convective boundary of the core is estimated by means of an algorithm which takes into account overshooting from the central convective region (Bressan, Chiosi & Bertelli 1981). In our formalism, the main parameter describing the overshoot is the mean free path of convective bubbles *across* the border of the convective region, expressed in units of pressure scale height, i.e. $\Lambda_{\rm c}$. Importantly, this parameter in the Bressan et al. (1981) formalism is not equivalent to others found in the literature. For instance, the overshooting scale defined by $\Lambda_{\rm c} = 0.5$ in the Padova formalism roughly corresponds to the 0.25 pressure scale height *above* the convective border, adopted by the Geneva group (Meynet et al. 1994, and references therein) to describe the same physical mechanism, i.e. $\Lambda_{\rm c}^{\rm G} = 0.25$.

It is well known that with this scheme, it is not possible to use a unique choice of the overshoot parameter independently of the stellar mass. This is particularly true for main sequence (MS) stars in the transition between models with radiative and convective cores, i.e. in the mass range between $M \sim 1.0$ and $\sim$1.5 $M_{\odot}$, depending on the adopted chemical composition. In this mass range, a strict application of the above overshoot criterion gives rise to the development of a convective core that grows too much with the evolution, producing a turnoff morphology which is not observed in the HR diagram (see the discussion in Aparicio et al. 1990). This is true also for the solar model for which the convective core would persist up to the present age of 4.6 Gyr, which is not supported by current interpretation of helioseismology observations.

We thus adopt a variable overshoot parameter $\Lambda_{\rm c}$ to describe the development of overshoot, in the transition from MS models with radiative and convective cores.

(i) $\Lambda_{\rm c}$ is zero for stellar masses $M \leq M_{\rm O1}$.

(ii) In the range $M_{\rm O1} \leq M \leq M_{\rm O2}$, we adopt a gradual increase of the overshoot efficiency with mass, from zero to $\Lambda_{\rm max}$. This is because the calibration of the overshooting efficiency in this mass range is still very uncertain due to the scarcity of stellar data provided by the oldest intermediate-age and old open clusters. Some works (Aparicio et al. 1990), however, indicate that this efficiency should be lower than in intermediate-mass stars.

(iii) For $M > M_{\rm O2}$, we adopt $\Lambda_{\rm c} = \Lambda_{\rm max}$.

At variance with previous releases (Bressan et al. 1993; Girardi et al. 2000; Bertelli et al. 2008), where the limiting masses $M_{\rm O1}$ and $M_{\rm O2}$ were fixed ($M_{\rm O1} = 1\,M_{\odot}$ and $M_{\rm O2} = 1.5\,M_{\odot}$), we now adopt a transition region that depends on the initial chemical composition of the model set. This allows for a better description of the effects of the elemental abundance on this phenomenon, which is needed because the onset of convective core overshoot leaves clear signatures that can be tested in observational colour–magnitude diagrams (CMD). The transition masses are automatically defined by running a preliminary subset of stellar tracks without diffusion, to check for the presence of a persistent convective unstable nucleus, without considering the overshoot (i.e. using the Schwarzschild criterion for convective borders). Since during the PMS phase the core may be already convective, we define the lower limit $M_{\rm O1}$ to be the minimum mass that is able to maintain this unstable core after 20 per cent of the initial hydrogen fraction has been burned in the centre.

$M_{\rm O1}$ varies with both metallicity and helium content. The bottom panel of Fig. 3 illustrates the behaviour of $M_{\rm O1}$ as a function of

Table 2. Nuclear reaction rates adopted in this work.

Reaction	Reference
$p\,(p\,,\beta^+\,\nu)\,D$	Cyburt et al. (2010)
$p\,(D\,,\gamma)\,^3He$	Descouvemont et al. (2004)
$^3He\,(^3He\,,\gamma)\,2\,p + ^4\,He$	Angulo et al. (1999)
$^4He\,(^3He\,,\gamma)\,^7Be$	Descouvemont et al. (2004)
$^7Be\,(e^-\,,\gamma)\,^7Li$	Caughlan & Fowler (1988)
$^7Li\,(p\,,\gamma)\,^4He + ^4He$	Descouvemont et al. (2004)
$^7Be\,(p\,,\gamma)\,^8B$	Angulo et al. (1999)
$^{12}C\,(p\,,\gamma)\,^{13}N$	Angulo et al. (1999)
$^{13}C\,(p\,,\gamma)\,^{14}N$	Angulo et al. (1999)
$^{14}N\,(p\,,\gamma)\,^{15}O$	Imbriani et al. (2005)
$^{15}N\,(p\,,\gamma)\,^4He + ^{12}C$	Angulo et al. (1999)
$^{15}N\,(p\,,\gamma)\,^{16}O$	Angulo et al. (1999)
$^{16}O\,(p\,,\gamma)\,^{17}F$	Angulo et al. (1999)
$^{17}O\,(p\,,\gamma)\,^4He + ^{14}N$	Chafa et al. (2007)
$^{17}O\,(p\,,\gamma)\,^{18}F$	Chafa et al. (2007)
$^{18}O\,(p\,,\gamma)\,^4He + ^{15}N$	Angulo et al. (1999)
$^{18}O\,(p\,,\gamma)\,^{19}F$	Angulo et al. (1999)
$^{19}F\,(p\,,\gamma)\,^4He + ^{16}O$	Angulo et al. (1999)
$^{19}F\,(p\,,\gamma)\,^{20}Ne$	Angulo et al. (1999)
$^{20}Ne\,(p\,,\gamma)\,^{21}Na$	Angulo et al. (1999)
$^{21}Ne\,(p\,,\gamma)\,^{22}Na$	Iliadis et al. (2001)
$^{22}Ne\,(p\,,\gamma)\,^{23}Na$	Hale et al. (2002)
$^{23}Na\,(p\,,\gamma)\,^4He + ^{20}Ne$	Hale et al. (2004)
$^{23}Na\,(p\,,\gamma)\,^{24}Mg$	Hale et al. (2004)
$^{24}Mg\,(p\,,\gamma)\,^{25}Al$	Iliadis et al. (2001)
$^{25}Mg\,(p\,,\gamma)\,^{26}Al^g$	Iliadis et al. (2001)
$^{25}Mg\,(p\,,\gamma)\,^{26}Al^m$	Iliadis et al. (2001)
$^{26}Mg\,(p\,,\gamma)\,^{27}Al$	Iliadis et al. (2001)
$^{26}Al^g\,(p\,,\gamma)\,^{27}Si$	Iliadis et al. (2001)
$^{27}Al\,(p\,,\gamma)\,^4He + ^{24}Mg$	Iliadis et al. (2001)
$^{27}Al\,(p\,,\gamma)\,^{28}Si$	Iliadis et al. (2001)
$^4He\,(2\,^4He\,,\gamma)\,^{12}C$	Fynbo et al. (2005)
$^{12}C\,(^4He\,,\gamma)\,^{16}O$	Buchmann (1996)
$^{14}N\,(^4He\,,\gamma)\,^{18}F$	Görres et al. (2000)
$^{15}N\,(^4He\,,\gamma)\,^{19}F$	Wilmes et al. (2002)
$^{16}O\,(^4He\,,\gamma)\,^{20}Ne$	Angulo et al. (1999)
$^{18}O\,(^4He\,,\gamma)\,^{22}Ne$	Dababneh et al. (2003)
$^{20}Ne\,(^4He\,,\gamma)\,^{24}Mg$	Angulo et al. (1999)
$^{22}Ne\,(^4He\,,\gamma)\,^{26}Mg$	Angulo et al. (1999)
$^{24}Mg\,(^4He\,,\gamma)\,^{28}Si$	Caughlan & Fowler (1988)
$^{13}C\,(^4He\,,n)\,^{16}O$	Angulo et al. (1999)
$^{17}O\,(^4He\,,n)\,^{20}Ne$	Angulo et al. (1999)
$^{18}O\,(^4He\,,n)\,^{21}Ne$	Angulo et al. (1999)
$^{21}Ne\,(^4He\,,n)\,^{24}Mg$	Angulo et al. (1999)
$^{22}Ne\,(^4He\,,n)\,^{25}Mg$	Angulo et al. (1999)
$^{25}Mg\,(^4He\,,n)\,^{28}Si$	Angulo et al. (1999)

metallicity for the main set of models to be described in this paper (see Section 5). Note that the resolution in the M_{O1} determination is of $0.05\,M_\odot$, which is the typical mass spacing we adopt for low-mass stars. The minimum values of M_{O1}, of $\sim 0.95\,M_\odot$, occur at the extremes of very low and very high metallicities. M_{O1} is found to be $1.1\,M_\odot$ at solar metallicities, and reaches a maximum of $1.15\,M_\odot$ at $Z = 0.02$. These values are in good agreement with the lowest mass of a non-diffusive model with a convective core, equal to $1.14\,M_\odot$, found by Michaud et al. (2004) for assumed solar metallicities of either $Z = 0.0175$ or 0.0199. The decreasing trend of M_{O1} at lower metallicities can be explained by the larger luminosity at given mass that causes the star to have a more concentrated nuclear energy source, hence a higher radiative gradient in the core (e.g. Marigo et al. 2001).

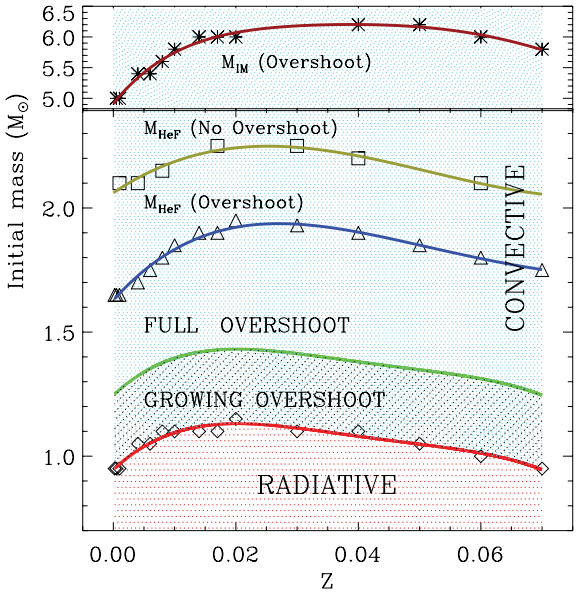

Figure 3. The behaviour of a few critical masses as a function of metallicity for our scaled-solar models following the $Y = 0.2485 + 1.78\,Z$ enrichment law (see Section 4). From bottom to top: the minimum mass that maintains a persistent convective core during H burning, M_{O1} (see the text for more details); the mass above which core overshoot is taken at the maximum efficiency M_{O2}; the minimum mass for a model to ignite central He non-degenerately, M_{HeF} for both the overshoot and the no-overshoot cases; finally, in the upper panel, the minimum mass of the stars that ignites C in a non-electron degenerate core, M_{IM}. The typical resolution in determining these mass limits is of $0.05\,M_\odot$ for M_{O1} and M_{HeF}, and of $0.2\,M_\odot$ for M_{IM}. The curves are polynomial fits to the corresponding values.

For the maximum overshooting efficiency, we adopt $\Lambda_{max} = 0.5$, i.e. a moderate amount of overshooting, which coincides with the values adopted in the previous Bertelli et al. (1994) and Girardi et al. (2000) models. This corresponds to about $0.25\,H_P$ of the overshoot region *above* the convective border found in other common formalisms.

M_{O2} is always set to be $M_{O1} + 0.3\,M_\odot$. This choice is motivated by the modelling of the open cluster M 67 (see Section 7 and Fig. 16), which indicates overshooting as efficient as $\Lambda_c \simeq 0.5$ already at masses of $\sim 1.3\,M_\odot$ for solar-metallicity stars. This choice is also supported by the Small Magellanic Cloud (SMC) cluster NGC 419 (Section 7 and Girardi, Rubele & Kerber 2009; Kamath et al. 2010), in which the turnoff probes masses between ~ 1.65 and $1.9\,M_\odot$.

Furthermore, we assume that the overshooting efficiency Λ_c increases linearly with mass between M_{O1} and M_{O2}, in order to ensure a smooth enough transition between the properties of stars with radiative and convective cores. This prescription has to be considered as a conservative approach that will be revisited in future works (e.g. Rubele et al. in preparation; Rosenfield et al. in preparation). The theoretical difficulties in defining the efficiency of overshooting in this transition region are well known (e.g. Aparicio et al. 1990). From the observational side, the recent indications from asteroseismology are still ambiguous: while the observations of α Cen A (de Meulenaer et al. 2010) suggest negligible overshooting in solar-metallicity stars of mass $\sim 1.1\,M_\odot$, recent asteroseismology studies of the nearby old low-mass star HD 203608 (Deheuvels et al. 2010), with $[Z/X] \simeq -0.5$, indicate the action of overshooting (with $\alpha_{ov} = 0.17$, which corresponds to $\alpha_{ov} \simeq 0.32$ in our formalism) at masses as low as $0.95\,M_\odot$, which is probably just slightly above the M_{O1}

limit. Clearly, the behaviour of overshooting in the transition region from M_{O1} to M_{O2} deserves more detailed investigations.

Another important difference with respect to previous releases of Padova evolutionary tracks is that the region of overshoot is considered to be radiative. In our original scheme, this region was assumed to be adiabatic while the majority of other authors took the overshoot region to be radiative. With the former assumption, the model adjusts the internal radiative temperature gradient in such a way that the unstable region is smaller than in the case of a radiative overshoot region. Thus, the effects of this new assumption are an overall larger mixed core. From a numerical point of view, this assumption provides a faster convergence, because the original formalism causes some instability during the convergence process that must be controlled.

In the stages of core helium burning (CHeB), the value $\Lambda_c = 0.5$ is used for all stellar masses. This amount of overshooting dramatically reduces the extent of the breathing pulses of convection found in the late phases of CHeB (see Chiosi, Bertelli & Bressan 1992).

2.6.2 *Overshoot in the convective envelope*

Alongi et al. (1991) were the first to consider the possibility that the base of the convective envelope can give rise to a sizable overshoot region. In the past, two important observational effects have been studied in relation with this phenomenon, namely the location of the RGB Bump in the red giant branch (RGB) of low-mass stars (globular clusters and old open clusters) and the extension of the blue loops of intermediate mass stars. Both effects have been found to be better explained by a moderate amount of overshoot, with a typical extension *below* the border of about $0.25-1.0\,H_P$. Against this possibility, it has always been argued that the calibration of the solar model does not require a sizable overshoot region because the transition between the fully adiabatic envelope and the radiative underlying region in our Sun is already well reproduced by models without overshoot. This however does not exclude the possibility that just below the fully adiabatic region, convection may penetrate in the form of radiative fingers that are even able to induce a significant mixing. Very recently it has been argued that a mechanism of this kind could even provide a better agreement with the physical state of matter in this transition region derived from solar oscillation data (Christensen-Dalsgaard et al. 2011). The size of this effect has been recently estimated to be $\Lambda_e \sim 0.4\,H_P$ but it is also consistent with a larger value $\Lambda_e \sim 0.6\,H_P$ which is in very good agreement with the one adopted since Alongi et al. (1991). As shown in Section 3 below, our own solar calibration suggests a value of Λ_e(Adiabatic) $\leq 0.05\,H_P$. We have not yet included the criterion adopted by Christensen-Dalsgaard et al. (2011). In view of the above results, we will maintain in this paper the same prescriptions adopted by Alongi et al. (1991) and Bressan et al. (1993): $\Lambda_e = 0.05$ in the envelope of stars with $M < M_{O1}$ and $\Lambda_e = 0.7$ in the envelope of stars with $M > M_{O2}$. In between we adopt a smooth transition similar to that used for the central overshoot in between these two limiting masses. Moreover, the temperature gradient in the envelope overshoot region is kept equal to the radiative one.

It is worth recalling that contrary to the overshoot in the central regions, the envelope overshoot has almost no effects on the evolutionary properties of the stars, though it may affect some observable properties, as already discussed. In this respect, an important observational evidence that we will investigate in the next future is the effect of the envelope overshoot on the abundance of light elements

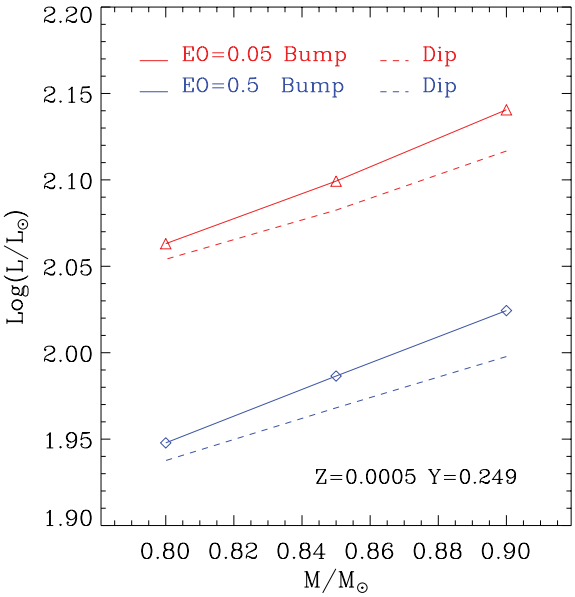

Figure 4. The luminosity both at the maximum (solid lines) and minimum ('dip', dashed lines) of the bump feature along the first-ascent RGB for a few low-mass tracks of $Z = 0.0005$, $Y = 0.249$ computed with $\Lambda_e = 0.05\,H_P$ (red) and $\Lambda_e = 0.5\,H_P$ (blue). In models with high Λ_e, the RGB bump is typically ∼0.3 mag fainter than in the model with negligible envelope overshooting.

(e.g. ^{7}Li), during and after the PMS evolution. To this purpose, one should also take into account that early MS stars could still suffer from a non-negligible mass accretion (De Marchi et al. 2011) and that envelope overshoot, during the PMS phase, could be more efficient than in the MS phase (Molaro et al. 2012). However, this is beyond the scope of this paper and will be addressed in a forthcoming investigation.

Another important effect of envelope overshooting is that of lowering the luminosity level of the bump along the first-ascent evolution of low-mass stars. Fig. 4 compares the bump luminosity between models computed with $\Lambda_e = 0.05\,H_P$ (red) and $\Lambda_e = 0.5\,H_P$ (blue) for a few low-mass tracks of composition ($Z = 0.0005$, $Y = 0.249$). In models with the higher Λ_e, the RGB bump is typically ∼0.3 mag fainter than in models with negligible envelope overshooting. By comparison, the observed RGB bump in globular clusters is about 0.2–0.4 mag fainter than that predicted by models without envelope overshooting (Di Cecco et al. 2010; see also Cassisi et al. 2011), though at the higher metallicities this result depends on the adopted metallicity scale. This simple comparison favours larger values of Λ_e in low-mass metal-poor stars than adopted here based on the solar calibration. Needless to say, this argument will be the subject of further calibrations.

2.6.3 *Breathing pulses and semiconvection*

During the end of the CHeB phase, models undergo a well-known instability, the breathing pulses. In a series of pulses of the helium core, a non-negligible fraction of the helium in the surrounding stable regions is brought and burned into the core. This causes an increase of the helium-burning lifetime which is not very significant by itself. But this has a dramatic effect on the duration of the subsequent AGB phase, which can be shortened by a significant factor. Given that this bears on the luminosity function of the brightest M and C stars, it is important to deal with this mechanism in the more

accurate and physically sound way as possible. At present there is no way to resolve the issue of whether this effect is numerical or real, because it happens independently from the adopted mixing scheme, i.e. with mild overshoot or with semi-convection. Work is in progress to calibrate the efficiency of this mechanism with observations.

2.6.4 Temperature gradient in the convective region

The energy transport in the convective regions is described according to the mixing-length theory of Böhm-Vitense (1958). The super-adiabatic gradient is maintained until its difference with respect to the adiabatic one decreases below $\nabla_{\rm Element} - \nabla_{\rm Adi} < 10^{-6}$. While in the convective core this condition is always fulfilled, in the convective envelope it is fulfilled only near the bottom of the region. The mixing length parameter $\alpha_{\rm MLT}$ is fixed by means of the solar model calibration performed below (see Section 3), and turns out to be $\alpha_{\rm MLT} = 1.74$. As already stated, the temperature gradient in any overshoot region is assumed to be the radiative one.

2.7 Mass meshing and other

The stellar structure equations are solved maintaining the algorithm of the fitting method. The fitting mass is typically set at $M/M_{\rm Tot} = 1 - 10^{-5}$, but it can be regulated on the basis of the corresponding temperature or depending on other needs. An adaptive mesh is used in the inner structure with a number of points that is about 1500 during hydrogen burning, 3000 during He burning and 5000 during the thermally pulsing AGB (TP-AGB).

As for the atmosphere, we adopt a plane-parallel grey model where the temperature stratification is given by a modified Eddington approximation for radiative transport:

$$T^4 = \frac{3}{4} T_{\rm eff}^4 \left[\tau + q\left(\tau\right)\right], \qquad (1)$$

where $\tau(r)$ is the optical depth and $q(\tau)$ is the Hopf function. Assuming the gas pressure P as the independent variable, the differential equation $\mathrm{d}\tau/\mathrm{d}\log P$ is solved by using a standard predictor-corrector method, starting from $\tau = 0$, where the gas pressure vanishes and the total pressure coincides with the radiation pressure to $\tau = \tilde{\tau}$, the latter being the optical depth of the photosphere. The overall method is fully described in Kippenhahn, Weigert & Hofmeister (1967).

We explicitly follow the evolution of 26 elements, listed in Section 2.4. The network of nuclear reactions is solved with a semi-implicit extrapolation scheme (Bader & Deuflhard 1983) that treats all nuclear reactions together and without any assumption on nuclear equilibria (see Marigo et al. 2001). At each time step the abundance equations are solved after each Henyey convergence, and particular care is paid both to maintain sufficiently small abundance variations (by adopting a suitably short time step) and to preserve the number of nucleons.

2.8 Diffusion

Microscopic diffusion is included following the implementation by Salasnich (1999). The diffusion coefficients are calculated following Thoul, Bahcall & Loeb (1994) and the corresponding system of second-order differential equations is solved together with the chemistry equation network, at the end of each equilibrium model. Diffusion is applied to all the elements considered in the code in the approximations that they are all fully ionized.

As already extensively discussed by Chaboyer et al. (2001), our knowledge of the diffusion process is still incomplete because if applied with the same diffusion constants used for the Sun in metal-poor stars of similar mass, they lead to surface abundance that are in disagreement with observations. Indeed, on the basis of accurate abundance determinations in stars of globular cluster NGC 6397 (Gratton et al. 2001), Chaboyer et al. (2001) concluded that microscopic diffusion should be fully inhibited in the external layers of metal poor stars at least down to a depth of about $0.005\,{\rm M}_\odot$ from the photosphere and partially inhibited down to $0.01\,{\rm M}_\odot$ from the photosphere.

In the case of metal-rich stars, microscopic diffusion in the external layers of stars of this mass is already inhibited by the more extended external convection. In general it is believed that when one considers more massive stars with less extended surface convective regions, the effects of diffusion are negligible because of the much shorter stellar evolutionary times. Even in this case, however, it can be shown that if the mesh spacing in the external layers is kept suitably small for accuracy purposes, diffusion can noticeably change the surface composition even for masses well above those of globular clusters if the external convection disappears. This in turn changes the interior opacities and produces somewhat unrealistic paths in the HR diagram, indicating that diffusion must be inhibited at the surface of these stars.

Other criteria can be used to deal with the particular problem of inhibiting molecular diffusion in those circumstances where its application would lead to evident discrepancies with observations. Surface abundances in stars without extended surface convective regions are very sensitive to the effects of atomic diffusion and radiative accelerations (Turcotte et al. 1998). However, in general it is found that some sort of extra-mixing beyond the base of the external convective layers must be added in order to reproduce the observed abundances (e.g. Richer, Michaud & Turcotte 2000). This extra-mixing, of unknown origin but whose effect is that of moderating/inhibiting other diffusive processes, is parametrized as a turbulent diffusion with a coefficient that is calibrated on the observed surface abundances of old stars (see e.g. VandenBerg et al. 2012, and references therein). Unfortunately, when the calibrating observable is the surface Li abundance, the results of different investigations, based on different stars, do not agree (Meléndez et al. 2010; Nordlander et al. 2012). Furthermore, this calibration is challenged even more by the discovery that early MS stars still suffer from a non-negligible mass accretion (De Marchi et al. 2011). This tail of accretion, preceded by a very efficient turbulent mixing during the PMS phase that completely destroys Li, could reshape our view of the surface evolution of this element (Molaro et al. 2012), and likely require another different calibration of the inhibiting mechanism. In view of all the above reasons and since we neglect for the moment radiative levitation (Vauclair 1983), we switch off the diffusion process when the mass size of the external convection falls below a threshold mass that we assume to be $\Delta M_{\rm conv} = 0.5$ per cent of the total stellar mass. Moreover, diffusion is not considered in stars that develop a persistent convective core, i.e. when core overshoot is taken into account.

Fig. 5 illustrates the impact of diffusion on the hydrogen-burning lifetimes in low-mass metal-poor evolutionary tracks with chemical composition $Z = 0.0006$, $Y = 0.249$. From this figure we see that, with this criterion, the effect of diffusion becomes very small for masses above $\sim 0.9\,{\rm M}_\odot$, which corresponds to ages of about 6 Gyr. At the 12 Gyr ages typical of globular clusters (with turnoff masses slightly below $\sim 0.8\,{\rm M}_\odot$), the differences between diffusive and non-diffusive models become significant: for instance, for the same

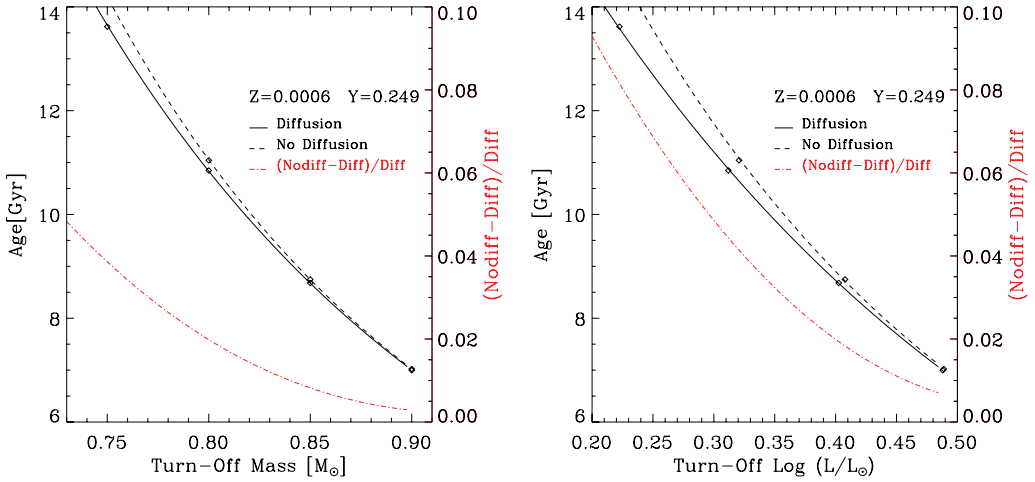

Figure 5. Comparison between the turnoff age as a function of the stellar mass for models with and without diffusion (dark lines) with the relative difference plotted in red (see the scale on the right-hand axis). The right-hand panel shows the same as a function of the turnoff luminosity. Differences between diffusive and non-diffusive models become negligibly small (less than 0.5 per cent in age) for masses above $\sim 0.9\,M_{\odot}$.

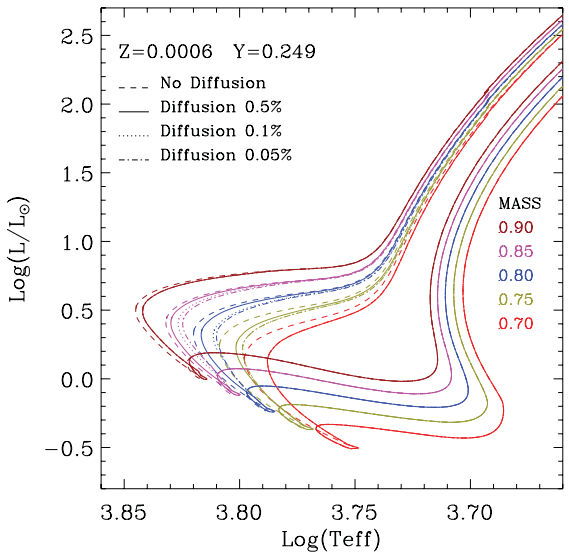

Figure 6. Comparison in the HR diagram between evolutionary tracks computed with different thresholds for turning-off diffusion, for a set of tracks of low masses and for a low metallicity of $Z = 0.0006$, $Y = 0.249$. Diffusion is switched off as soon as the mass size of the surface convection falls below the indicated fractional values of the total mass. For reference, the case without diffusion is also shown. See the text for more details.

turnoff luminosity, ages derived from non-diffusive models would be about 8 per cent older than those derived from diffusive models. These differences are perfectly in line with those found by other authors (Castellani & degl'Innocenti 1999, and references therein).

To explore the sensitiveness of the results to different values of the threshold for turning-off diffusion, we have also computed the cases with $\Delta M_{\rm conv}$ =0.1 and 0.05 per cent for the same chemical composition $Z = 0.0006$, $Y = 0.249$. All the above cases are displayed in Fig. 6. Decreasing the threshold mass delays the quenching of diffusion and produces a larger shift of the turnoff region towards cooler temperatures. This effect is more pronounced in the mass range between 0.85 and $0.75\,M_{\odot}$. At lower masses, surface convection is always well developed while at higher masses convection rapidly disappears. However, we note that in the latter case this result is also due to the inhibition of diffusion throughout the whole star, an assumption that could be improved following recent investigations that underline the importance of turbulent mixing in the more external regions (see e.g. VandenBerg et al. 2012). In the light of these considerations, we plan a revision of the tracks in this mass and metallicity range in the near future (see note added in proof).

3 CALIBRATION OF THE SOLAR MODEL

The comparison with the solar model is a necessary step to check the quality of the input physics and to calibrate some parameters that cannot be derived from the theory.

For this purpose, we have computed a large grid of tracks of $1\,M_{\odot}$, from the PMS phase to an age of 4.8 Gyr, and varying the initial composition of the Sun, $Z_{\rm initial}$ and $Y_{\rm initial}$, the mixing length parameter $\alpha_{\rm MLT}$ and the extent of the adiabatic overshoot at the base of the convective envelope $\Lambda_{\rm e}$. To calibrate these free parameters, the models were compared with a set of solar data obtained from the literature which are summarized in Table 3. The reference solar data used here come from *SOHO* Michelson Doppler Imager (MDI) observations described in Basu et al. (2000). More recent data can be found in Basu et al. (2009) from the Birmingham Solar Oscillation Network (BiSON) experiment. However, since we wish to compare our model with previous ones in the literature, in particular considering the effects of changing the present day surface solar composition, we have found it more convenient to use Basu et al. (2000) data, with respect to which there are several comparisons at different chemical compositions made in the literature. Besides verifying the performance of our solar model, another goal of the comparison is to obtain the mixing length parameter, $\alpha_{\rm MLT}$, that will be used to compute all the stellar evolutionary sets. For this reason, the calibration has been obtained exactly with the same set-up used for the calculations of the other tracks, i.e. with tabulated EOS and opacities and, of course, using microscopic diffusion. However, in order to check the effects of interpolating the EOS, we have also computed a solar model with the 'on-the-fly' version of FREEEOS. In this model we have adopted the parameters of the best fit obtained with the tabulated EOS, and we changed only the solar age in order to match as much as possible the solar data. The parameters of our best model are listed in the lower part of Table 3.

In the left-hand panel of Fig. 7, we plot the relative variation of the squared sound speed $\delta c_{\rm s}^2/c_{\rm s}^2$ as a function of the fractional radius

Table 3. Solar calibration.

Solar data	Value	Error	Source
$L_\odot$ (10^{33} erg s^{-1})	3.846	0.005	Guenther et al. (1992)
$R_\odot$ (10^{10} cm)	6.9598	0.001	Guenther et al. (1992)
$T_{\rm eff,\odot}$ (K)	5778	8	From $L_\odot$ and $R_\odot$
$Z_\odot$	0.015 24	0.0015	Caffau et al. (2011)
$Y_\odot$	0.2485	0.0035	Basu & Antia (2004)
$(Z/X)_\odot$	0.0207	0.0015	From $Z_\odot$ and $Y_\odot$
$R_{\rm ADI}/R_\odot$	0.713	0.001	Basu & Antia (1997)
$\rho_{\rm ADI}$	0.1921	0.0001	Basu et al. (2009)
$C_{\rm S,ADI}/10^7$ cm sxyd	2.2356	0.0001	Basu et al. (2009)
Model	Tab-EOS	Fly-EOS	
Age[a](Gyr)	4.593	4.622	
$Z_{\rm initial}$	0.017 74	0.017 74[b]	
$Y_{\rm initial}$	0.28	0.28[b]	
$\alpha_{\rm MLT}$	1.74	1.74[b]	
$\Lambda_{\rm e}$	0.05	0.05[b]	
L (10^{33} erg s^{-1})	3.848	3.841	
R (10^{10} cm)	6.9584	6.961 12	
$T_{\rm eff}$ (K)	5779	5775	
$Z_{\rm S}$	0.015 97	0.015 95	
$Y_{\rm S}$	0.247 87	0.247 62	
$(Z/X)_\odot$	0.021 69	0.021 66	
$R_{\rm ADI}/R_\odot$	0.7125	0.7129	
$\rho_{\rm ADI}$	0.1887	0.1881	
$C_{\rm S,ADI}/10^7$ cm s^{-1}	2.2359	2.2364	

Distribution of heavy elements from Caffau et al. (2011).
[a]Age includes the PMS phase.
[b]Values taken from the calibration obtained with tabulated EOS.

inside the Sun (red crosses and solid line). The sense of the comparison is (Sun−model)/Sun in both panels. The Solar values were obtained from MDI data (Basu et al. 2000). In the same figure, we also show the Basu et al. (2009) model differences with respect to MDI data, obtained with the Grevesse & Sauval (1998) solar abundances (blue diamonds), and the Serenelli et al. (2009) difference profile using Grevesse & Sauval (1998) solar abundances (black squares) and using Asplund et al. (2009) solar abundances (green triangles). In the right-hand panel, we show the relative variation of the density profile (red crosses and solid line) and we compare it only with the Basu et al. (2009) difference profile (blue diamonds). Note that the quoted age includes the PMS lifetime, which when determined by the stage on the zero age main sequence (ZAMS) where the total gravitational luminosity goes to zero, amounts to about 40 Myr. Inspection of Table 3 and of Fig. 7 shows that our solar model performs fairly well, taking also into account that lowering the solar metallicity from the Grevesse & Sauval (1998) values had a severe impact in the performance of the solar model. Particularly interesting are the small values of the $\delta c_{\rm s}^2/c_{\rm s}^2$ and density profiles in the central radiative regions of the Sun, indicating that good agreement is also possible with abundances lower than those of Grevesse & Sauval (1998). Towards the central region, our model suffers from a slightly lower sound speed and a slightly lower density than shown by the solar data. A similar though less pronounced problem is also present in the comparison of models with Solar data extracted from the BiSON experiment (Basu et al. 2009).

For the track computed with the 'on-the-fly' FREEEOS, we did not repeat the calibration process; thus, it does not reproduce the basic solar data of Table 3 as well as in the previous case. However, we see that we may also obtain a fairly good agreement with solar data, by slightly increasing the age.

From the initial values of the metallicity and helium abundance of the Sun, $Y_{\rm initial}$, $Z_{\rm initial}$ and adopting for the primordial He abundance $Y_{\rm p} = 0.2485$ (Komatsu et al. 2011), we also obtain the helium-to-metals enrichment ratio, $\Delta Y/\Delta Z = 1.78$. This value will be used in the following to determine the default value of helium content for any given global metallicity.

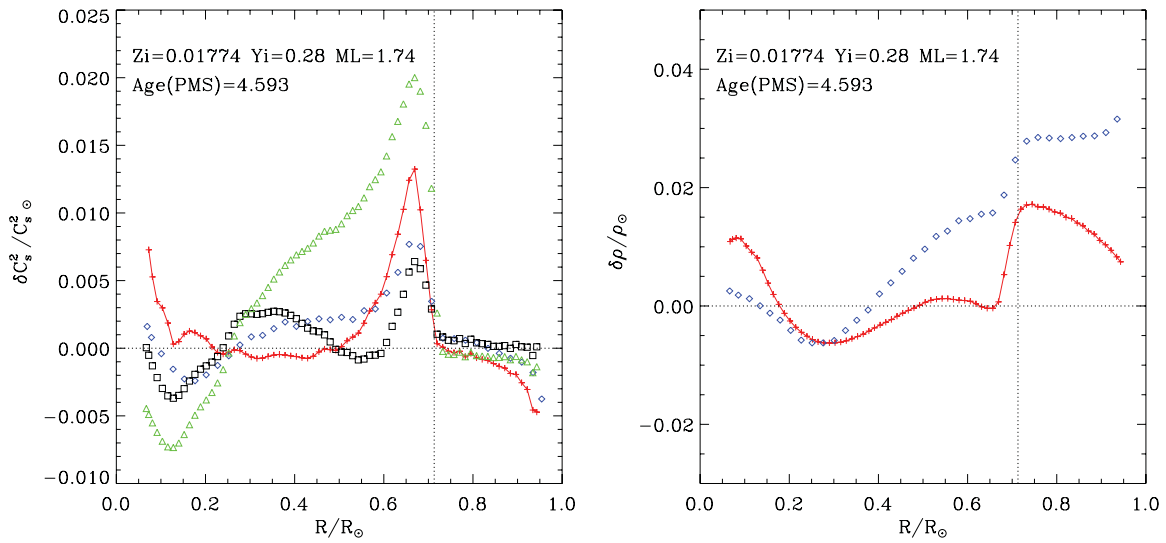

Figure 7. Solar model obtained using the tabulated FREEEOS. Left-hand panel: interior relative differences (in the sense Sun minus model) in the squared sound speed $\delta c_{\rm s}^2/c_{\rm s}^2$. Solar values are obtained from MDI data (Basu, Pinsonneault & Bahcall 2000). Symbols are as follows. Red crosses: our model; blue diamonds: Basu et al. (2009) model differences with respect to MDI data using Grevesse & Sauval (1998) solar abundances; black squares: Serenelli et al. (2009) using Grevesse & Sauval (1998) solar abundances; green triangles: Serenelli et al. (2009) using Asplund et al. (2009) solar abundances. Right-hand panel: interior relative differences for the density profile. In this case, only the Basu et al. (2009) model is shown for comparison. Z_i, Y_i and ML refer to the initial metallicity and helium abundance and to the $\alpha_{\rm MLT}$ of our model, respectively. The quoted age includes the PMS lifetime which is about 40 Myr, determined by the stage on the ZAMS where the total gravitational luminosity falls, and remains, below a few per cent. Values obtained from this calibration are shown in Table 3.

Table 4. Initial chemical composition of the sets ready at the time of this writing.

			[α/Fe] (dex)		
Z	Y	[M/H][a]	0	+0.2	+0.4
0.0005	0.2485	−1.49	×	×	
0.001	0.250	−1.19	×	×	
0.004	0.256	−0.58	×	×	
0.005	0.258	−0.48			×
0.006	0.259	−0.40	×	×	
0.008	0.263	−0.28	×	×	
0.010	0.267	−0.18	×	×	×
0.010	0.263	−0.18		×	
0.014	0.273	−0.02	×		
0.015	0.276	−0.01		×	
0.017	0.279	+0.06	×	×	
0.017	0.350	+0.11	×		
0.017	0.400	+0.15	×		
0.02	0.284	+0.14	×	×	×
0.03	0.302	+0.34	×	×	
0.04	0.321	+0.48	×	×	
0.05	0.339	+0.60	×	×	
0.06	0.356	+0.70	×	×	×
0.07	0.375	+0.78	×	×	

[a]Approximated value from [M/H] = log ((*Z*/*X*)/0.0207).

4 INITIAL CHEMICAL COMPOSITION OF THE EVOLUTIONARY TRACKS

As already specified in Section 2.1, our selected reference distribution of heavy elements is taken from Grevesse & Sauval (1998), except for a subset of species for which we adopt the recommended values according to the latest revision by Caffau et al. (2011).

For the present release, other distributions have been considered such as those typical of the Large Magellanic Cloud, of massive early-type galaxies and of α-depleted elements.

The helium and metal mass fractions are chosen according to the relation $Y = 0.2485 + 1.78\,Z$ obtained from the solar calibration. Sets with varying helium at fixed metallicity are also considered.

We recall here that when we change the fractional abundance by the number of heavy elements to obtain a new distribution, their fractional abundance by mass is re-normalized in such a way that the global metallicity, Z, is kept constant.

Full sets of opacity and EOS tables are recomputed for each different chemical composition. Chemical compositions for which we have already computed full sets of evolutionary tracks are shown in Table 4. More sets are being computed for α-enhanced distributions.

5 STELLAR TRACKS

A complete set of evolutionary tracks in the HR diagram is shown in Fig. 8, for the chemical composition $Z = 0.008$, $Y = 0.263$ with $[\alpha/\mathrm{Fe}] = 0$. Such plots are available for all sets listed in Table 4.

5.1 Mass range

In this paper, we present the evolution of stars with initial mass between 0.1 and 12 $\mathrm{M}_\odot$. Higher stellar masses will be considered in a future paper. The mass spacing is smaller than in previous releases, being typically of 0.05 $\mathrm{M}_\odot$ in the range of low-mass stars and ∼0.2 $\mathrm{M}_\odot$ for intermediate-mass stars. This allows a good description of the transition between low- and intermediate-mass stars, and between intermediate- and high-mass stars.

5.2 Pre-main sequence

The PMS evolution is a new characteristic of this release and it is implemented as follows. A stellar model with suitable mass and initial composition is obtained along the Hayashi track and artificially expanded until its central temperature falls below $T_\mathrm{c} \approx 10^5$ K. At this stage, no nuclear reactions are active and the model is fully convective and homogeneously mixed. From this configuration, we allow the star to evolve at constant mass along the PMS contraction and subsequent phases. The PMS phase of $Z = 0.008$, $Y = 0.263$, $[\alpha/\mathrm{Fe}] = 0$ tracks is shown in Fig. 8.

The typical PMS lifetimes are illustrated in Fig. 9, as a function of stellar mass and for two different metallicities. It can be noticed that the behaviour as a function of mass is very regular just for masses higher than about 1 $\mathrm{M}_\odot$. For smaller masses, the higher relative importance of the deuterium burning, and the onset of completely convective stars at $M \lesssim 0.4\,\mathrm{M}_\odot$, causes the behaviour to be less monotonic. Also it should be mentioned that the definition of what is PMS phase is not so straightforward, so that in some cases we find some small glitches in the mass–PMS lifetime relation, even at higher masses. These features seem to be less of a problem while making the isochrones for the PMS phase.

5.3 Other evolutionary stages

During the PMS evolution a number of low-temperature reactions change the abundance of some light elements and the model is no longer homogeneous. The end of this phase is also characterized by a rapid reassessment of the internal structure during which the evolutionary track in the HR diagram shows characteristic patterns (loops) that depend on the initial mass and on the initial chemical composition. The above effects render difficult the identification of the ZAMS point in an unambiguous way. To define the beginning of the MS, we thus consider the point where the evolutionary speed in the HR diagram shows an abrupt drop, decreasing by more than two orders of magnitude in a very short time. This point is clearly detectable in all tracks and it will also be used to define the beginning of the MS when constructing the corresponding isochrones.

Very low mass stars with mass $M \leq 0.45\,\mathrm{M}_\odot$ are evolved up to an age of 100 Gyr. Some test models have been evolved up to the central hydrogen exhaustion and subsequent core degenerate phase, when the model abandon the RGB because the hydrogen shell reaches the surface of the star. These tracks show some interesting features but of course are not of any interest for single stellar evolution because the age where these features happen is by far larger than the Hubble time.

Low-mass stars, with mass between $M \sim 0.5\,\mathrm{M}_\odot$ and an upper value (M_HeF), which mainly depend on the chemical composition and on the eventual extra mixing in the convective nucleus, ignite helium in an electron degenerate hydrogen-exhausted core and undergo the so-called He-flash. When the He-burning luminosity exceeds the stellar surface luminosity by a factor of 200, the track is interrupted and the following evolution along the central helium-burning phase is computed separately. The He-burning phase of low-mass stars is re-started from a suitable zero age horizontal branch (ZAHB) model with the same core mass and internal and surface chemical composition as the last RGB model. The evolution is thus followed up to well-developed thermal pulses on the AGB.

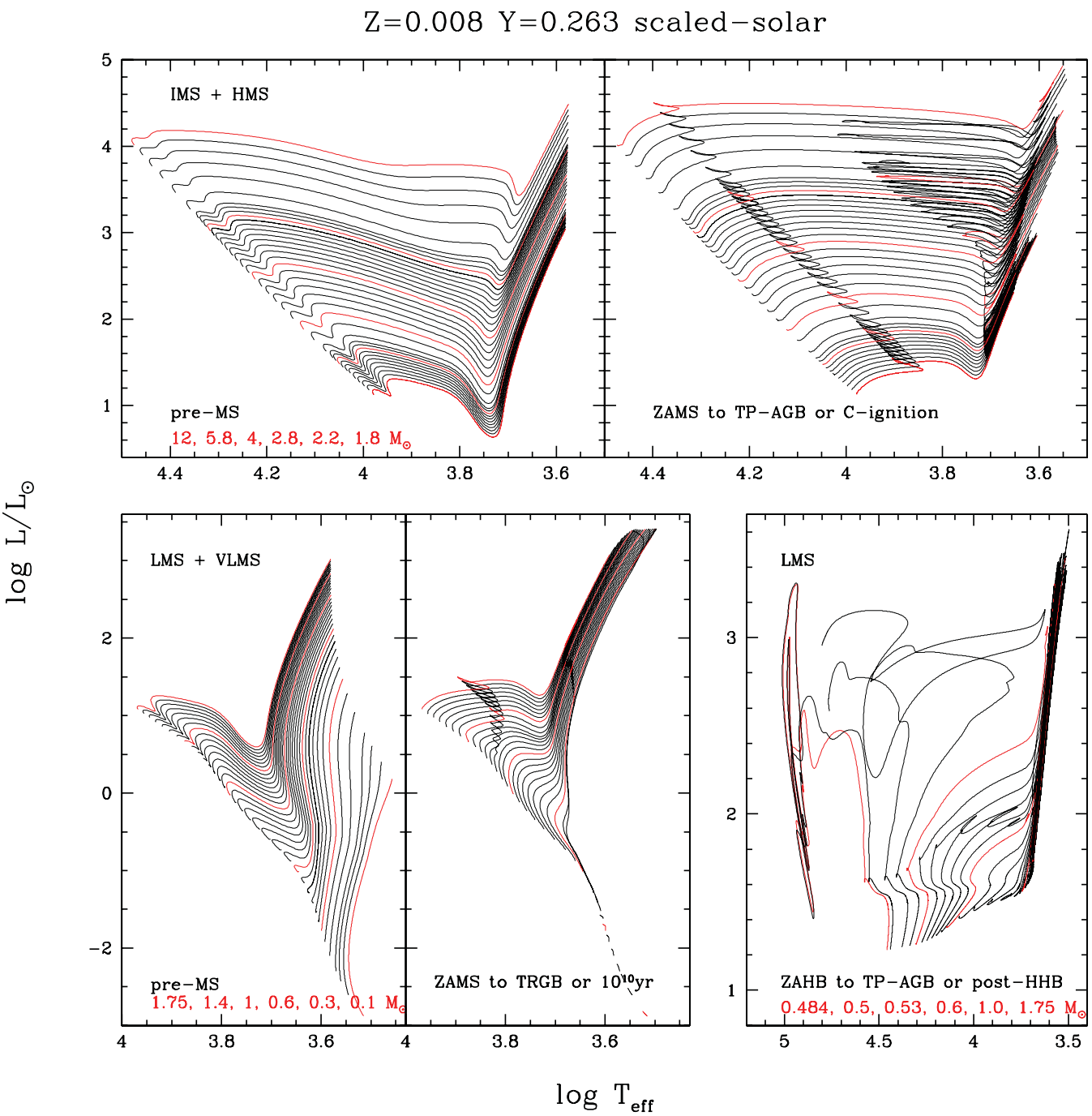

Figure 8. Evolutionary tracks in the HR diagram for the selected chemical composition $Z = 0.008$, $Y = 0.263$ and with $[\alpha/\mathrm{Fe}] = 0$. The upper panels show the tracks for intermediate- and high-mass stars (IMS+HMS) split into the PMS and later evolution; in the latter case, the evolution is followed until the beginning of the TP-AGB, or up to C-ignition for $M > 5.8\,\mathrm{M}_{\odot}$. The low and very low mass stars (LMS+VLMS) are shown in the bottom-left panels. In this case, the evolution after the PMS is plotted either up to the tip of the RGB, or up to an age of 100 Gyr for $M < 0.6\,\mathrm{M}_{\odot}$. The bottom-right panel shows the complete suite of low-mass He-burning tracks computed for this set. The evolution starts at the ZAHB sequence and goes up to either the beginning of the TP-AGB for $M > 0.6\,\mathrm{M}_{\odot}$, or up to the stages of post-early AGB, and AGB-manqué (and in some cases including the initial dimming towards the white dwarf sequence), typical of lower mass HB stars that follow a hot-HB evolution (HHB).

The subsequent TP-AGB evolution up to the complete ejection of the envelope will be presented in an accompanying paper (Marigo et al. in preparation).

In the construction of the initial ZAHB model, we take into account that a fraction of the helium in the convective core has been burned into carbon during the He flash. This fraction is estimated as the amount of nuclear fuel necessary to lift the core degeneracy and is computed for each track. It closely follows the total mass of the core at the HeF, as illustrated in Fig. 10.

For masses larger than M_{HeF}, we follow the evolution either until the first few (5–20) well-developed thermal pulses along the AGB (in which case the star belongs to the range of intermediate-mass stars) or until central carbon ignition for higher mass models (in which case the star is broadly defined a massive star). For a given

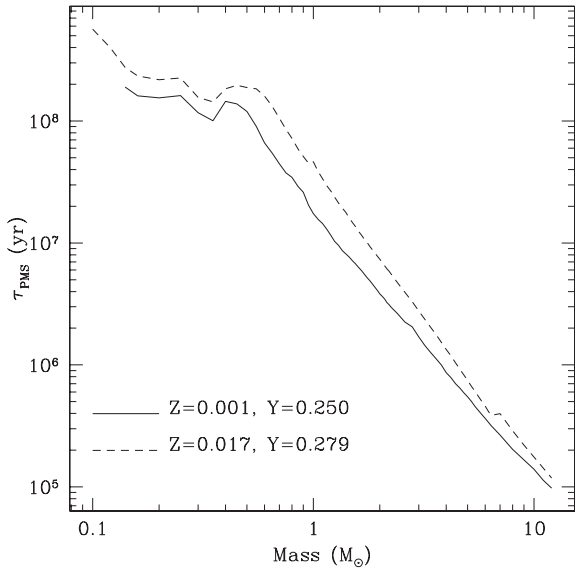

Figure 9. PMS lifetimes, as a function of stellar mass and for two different metallicities.

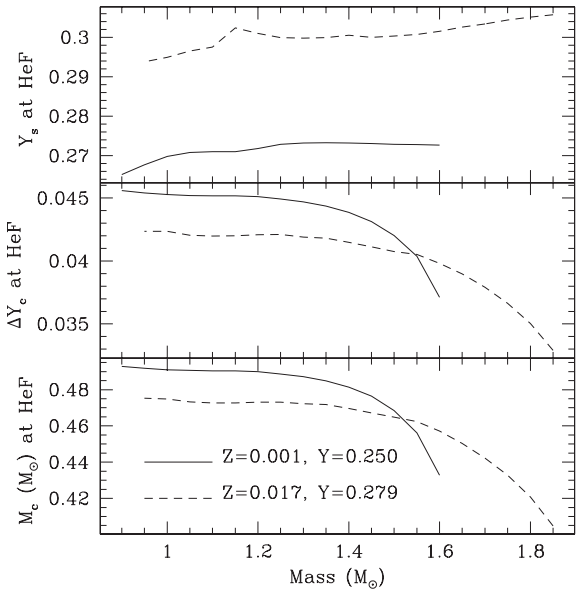

Figure 10. Quantities that primarily determine the properties of He-burning low-mass stars, as a function of mass and for two solar-scaled chemical compositions. Bottom panel: the core mass at the moment of the He flash. Middle panel: the same for the mass fraction of helium, ΔY_c, that is burned into carbon to provide the energy to lift electron degeneracy in the core, between the RGB tip and ZAHB models. Top panel: the same for the mass fraction of helium in the envelope.

input physics (i.e. opacities, neutrino losses, etc.), the separation mass between the two classes, $M_{\rm IM}$, depends on the chemical composition and degree of convective core extra mixing.

The values of $M_{\rm HeF}$ and $M_{\rm IM}$ as a function of metallicity are illustrated in Fig. 3 for our grids of scaled-solar tracks. As can be noticed, the behaviour of $M_{\rm HeF}$ closely follows the one of $M_{\rm O1}$ (Section 2.6.1), with a maximum at intermediate metallicities. About the same happens for $M_{\rm IM}$, but with the maximum values – of $\sim$6 $M_\odot$ – moving to higher metallicities.

5.4 α-enhanced mixtures

Fig. 11 exemplifies the effect of adopting α-enhanced mixtures on the evolutionary tracks in the H–R diagram. There is a systematic trend of the α-enhanced tracks (blue line) to be somewhat warmer than the corresponding scaled-solar cases (red line), especially along the RGB.

In this respect, we call attention to the fact that the effect of the α-enhancement depends critically on the way the chemical mixture is effectively built. In general, given an [α/Fe] ratio, one has two options: (a) either keeping the ratio [Fe/H] fixed while increasing the absolute abundances of the α elements, which leads to a net increase of the total metallicity Z, or (b) keeping the metallicity Z fixed while depressing the abundances of the Fe-group elements and somewhat enhancing those of the α elements. The tracks presented in Fig. 11 are computed with the (b) option. In the latter case, the most relevant consequence is the effective increase of O, Mg, Ne, etc., while in the former case the most important effect is the depletion of the Fe-group elements.

The changes in the abundances may produce important effects on evolutionary tracks, mainly due to opacity effects. We recommend to refer to Marigo & Aringer (2009) for a thorough discussion of this issue (in particular their sections 4.3, 4.4 and figs 20, 21 and 22).

As a general rule, we may expect that α-enhanced tracks computed according to the (a) option tend to be cooler than the corresponding scaled-solar tracks (see e.g. VandenBerg et al. 2012) because of a net increase in the metallicity, while α-enhanced tracks computed according to the (b) option tend to be cooler than the corresponding scaled-solar tracks because the depression of the Fe-group elements implies a reduction of the H^- opacity, important absorption source at temperatures $\approx$3000–6000 K. In fact, the H^- opacity is highly sensitive to the number of free electrons, a significant fraction of which is just provided by Fe-group elements.

5.5 Comparison with previous releases

In Fig. 12, we compare our new tracks with the corresponding ones selected from a few previous releases from Padova, in order to give the reader an immediate impression of the similarities and differences brought by the updates in input physics. The selected composition is that typical of young populations in the Large Magellanic Cloud. The metallicity is $Z = 0.008$ for all the tracks but the helium abundance Y may be slightly different among the different sets.

Besides the presence of the PMS in the new tracks, a few general trends can be seen in the figure.

First of all, the effect of diffusion is clearly visible in the tracks of lower mass. If we allow for a small shift in the ZAMS caused by the different input physics, we see that the new track runs cooler during the MS, and have a cooler turnoff. Another evident and important difference in low-mass stars is that the base of the RGB is bluer in the new tracks. The two effects above will clearly affect the age determination of old populations, whenever the effective temperatures are used to constrain their ages.

Moreover, with respect to Girardi et al. (2000), the RGB itself is less steep and runs at lower temperatures. In this phase, the differences with respect to Bertelli et al. (2008) are less marked and the tracks have a very similar slope.

In the intermediate mass stars ($M = 5\,M_\odot$), the models show significant differences already from the MS. These differences are mainly due to the larger He abundance of the new tracks, and we

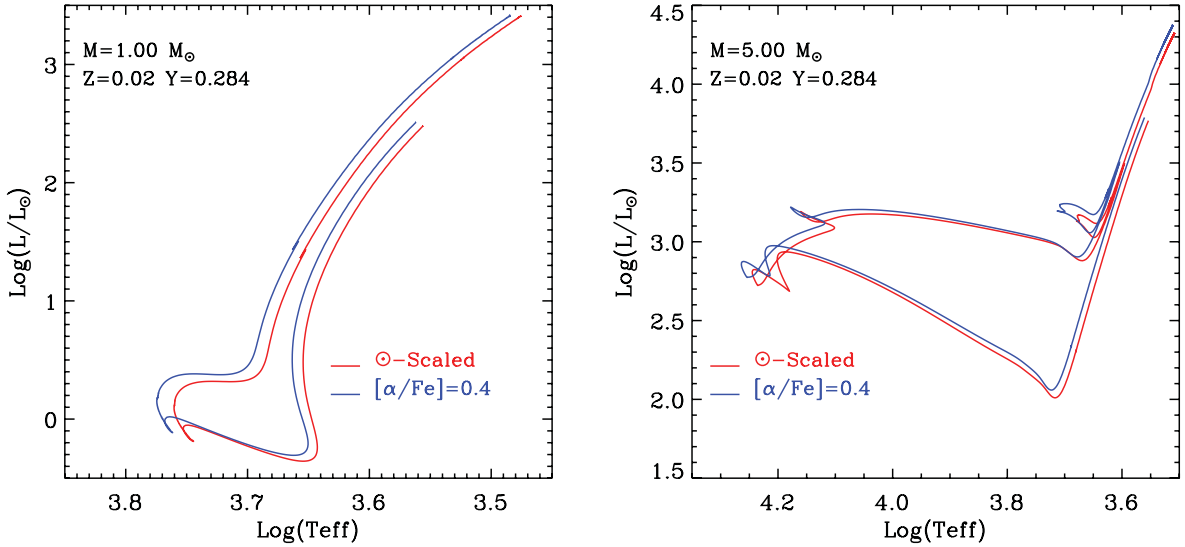

Figure 11. Comparison between evolutionary tracks computed either with scaled-solar chemical composition, or α-enhanced mixtures, while keeping the same initial total metallicity Z and helium content Y. Stellar masses (in $M_{\odot}$) are indicated in each plot.

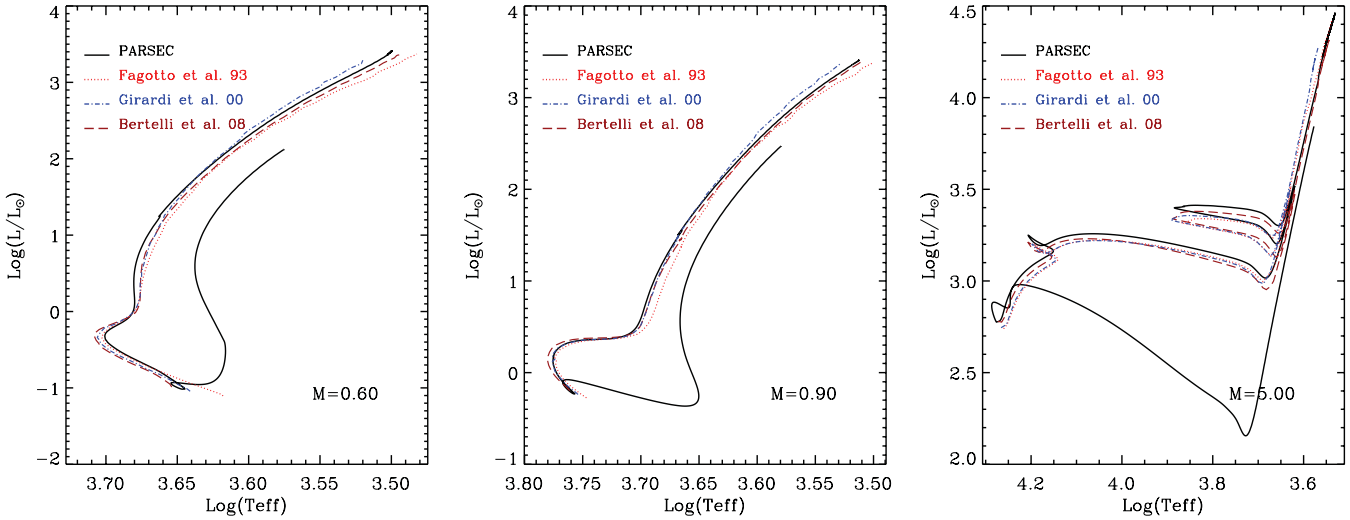

Figure 12. Comparison with previous releases of Padova evolutionary tracks with $Z = 0.008$. Note that He abundances are slightly different among the different sets illustrated: $Y = 0.263$ for PARSEC; $Y = 0.25$ for Fagotto et al. (1994); $Y = 0.25$ for Girardi et al. (2000); $Y = 0.26$ for Bertelli et al. (2008).

limit the comparison only to the Bertelli et al. (2008) set, which has almost the same composition. In this case, we can see that the new track runs slightly more luminous not only in the MS but also in the post-MS phases. This is mainly due to the different assumption about the value of the real temperature gradient in the overshoot region. Bertelli et al. (2008) assume that the overshoot region is adiabatic. The consequence of this assumption in the equilibrium structure is that the Schwarzschild unstable core is less extended and thus it renders the extra mixing (with the same overshoot parameter) less efficient. In other words, assuming that the overshoot region is radiative is equivalent to assuming a slightly larger overshoot parameter and, correspondingly, the star evolves at a higher luminosity because of the larger mixed core.

We notice again that the red giant phase – in this case the early AGB – in the new tracks is significantly cooler than in Girardi et al. (2000). This difference is important because it bears on the mass-loss rates and thus on the subsequent evolution of the stars along the TP-AGB.

5.6 Comparison with other data bases

There are several large data bases of stellar evolutionary tracks available in the literature. All them differ in several important aspects, including the adopted solar chemical composition and calibration, the sources of opacities and EOS, the coverage of evolutionary phases, the extension in the metal–helium content plane, etc. Comparing all these tracks is not among our goals. We limit ourselves to a few comparisons that point to the important similarities and differences between some recent libraries.

Fig. 13 compares the He core mass and the luminosity at the He flash (or, equivalently, at the tip of the RGB), with those provided in the Dartmouth (Dotter et al. 2008), Pisa (Dell'Omodarme et al. 2012) and BaSTI (Pietrinferni et al. 2004) data bases. It is evident that although the initial helium content in not exactly the same among these tracks, the PARSEC models agree very well with the most recent Pisa ones, and follow the same trend as the Dartmouth ones – with just small offsets, of a few 0.001 $M_{\odot}$ in

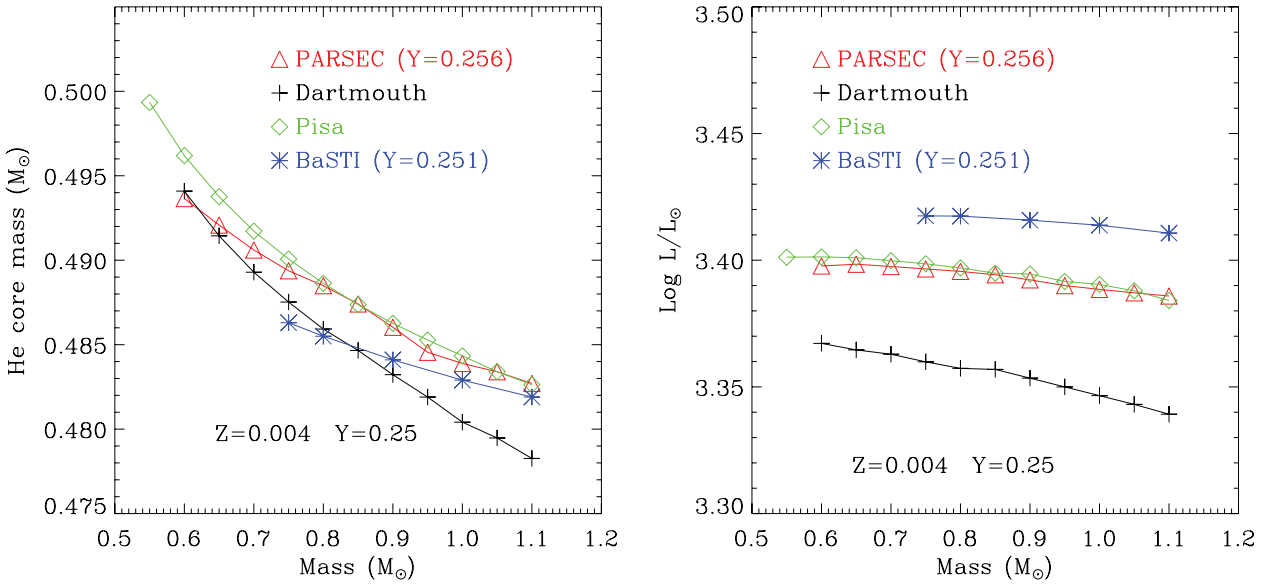

Figure 13. He core mass (left-hand panel) and luminosity (right-hand panel) at the tip of the RGB. The PARSEC models for $Z = 0.004$, $Y = 0.256$ are compared with those from other authors, namely Dotter et al. (2008, Dartmouth), Dell'Omodarme et al. (2012, Pisa) (both with $Z = 0.004$, $Y = 0.250$) and Pietrinferni et al. (2004, BaSTI) (with $Z = 0.004$, $Y = 0.251$).

the He core mass, and a few 0.01 dex in luminosity. This general agreement is very encouraging. It is also interesting to note that, although presenting offsets of similar magnitude, the BaSTI tracks have a different behaviour, with slightly smaller core masses being followed by slightly larger luminosities at the tip of the RGB.

As an illustration of the possible differences in the HR diagrams, Fig. 14 compares PARSEC with BaSTI tracks (Pietrinferni et al. 2004), using always the same chemical composition of $Z = 0.0198$, $Y = 0.2734$. This is the initial solar composition in BaSTI, obtained from Grevesse & Sauval (1998) and their calibration of the solar model, which results in a mixing length parameter of $\alpha_{\rm MLT} = 1.913$. The straight computation of PARSEC stellar evolutionary tracks with the same Z, Y and $\alpha_{\rm MLT}$ results in tracks very similar to BaSTI, as can be appreciated comparing the red (BaSTI) with the blue lines (PARSEC). However, the bulk of present PARSEC tracks is calculated with our own solar-calibrated $\alpha_{\rm MLT} = 1.74$. PARSEC tracks with $\alpha_{\rm MLT} = 1.74$ are presented in green. They appear significantly cooler than the BaSTI tracks, especially at the RGB. This significant difference results mainly from the lower metallicities assumed for the solar model in PARSEC and the calibration of $\alpha_{\rm MLT}$.

This example illustrates how risky is the straight comparison between tracks computed with a different solar composition and calibration.

5.7 Data tables

The data tables for the present evolutionary tracks are available in electronic format only through our websites.[7] For each evolutionary track, the corresponding data file presents at least 50 columns with the run of many quantities of interest along the track, as described in a suitable *ReadMe* file.

[7] http://stev.oapd.inaf.it/parsec_v1.0

6 ISOCHRONES

For the sake of completeness we present here, together with the set of evolutionary tracks, also the corresponding isochrones. These isochrones do not contain either the TP-AGB or the post-AGB phases. These are discussed in accompanying papers dealing with the extension of the tracks into these advanced phases (e.g. Marigo et al. in preparation), and their calibration (basically in terms of third dredge-up and mass-loss efficiencies) on the base of a large set of observational data. Although we can ensure a quick initial calibration of the TP-AGB phase following the procedure defined by Marigo & Girardi (2007), a thoroughful calibration may require a significant time before completion. We thus focus here our attention on the less advanced phases of stellar evolution which are, nevertheless, important thanks to the huge amount of observational data they can help to interpret.

Following Bertelli et al. (1994), isochrones are computed by first dividing the evolutionary tracks in suitable homogeneous evolutionary phases. The isochrones are then constructed by interpolating points along missing stellar tracks, between the corresponding phases of the calculated grid masses. The points that separate the selected evolutionary phases along the tracks are automatically recognized by a suitable algorithm that takes into account both the morphology in the HR diagram and the interior physics. We store the full track information for the purpose of constructing isochrones even in non-conventional diagrams, like for example in the surface composition of some particular elements.

Examples of isochrones in the HR diagram are shown in Fig. 15 for the sets with scaled-solar chemical composition that follow the relation $Z = 0.2485 + 1.78\,Z$. For these sets, isochrones can already be built for any age from ∼1 Myr to at least 20 Gyr (limited to the mass interval $0.1 \leq M \leq 12\,{\rm M}_{\odot}$) and for any metallicity in the range $0.0005 \leq Z \leq 0.07$ (corresponding to $-1.49 \leq [{\rm M/H}] \leq +0.78$). We also note the presence of the PMS in the isochrones with the youngest ages. Mass loss by stellar winds has been considered only during the RGB of low-mass stars, using the empirical formula by Reimers (1975) multiplied by an efficiency factor η. The latter is

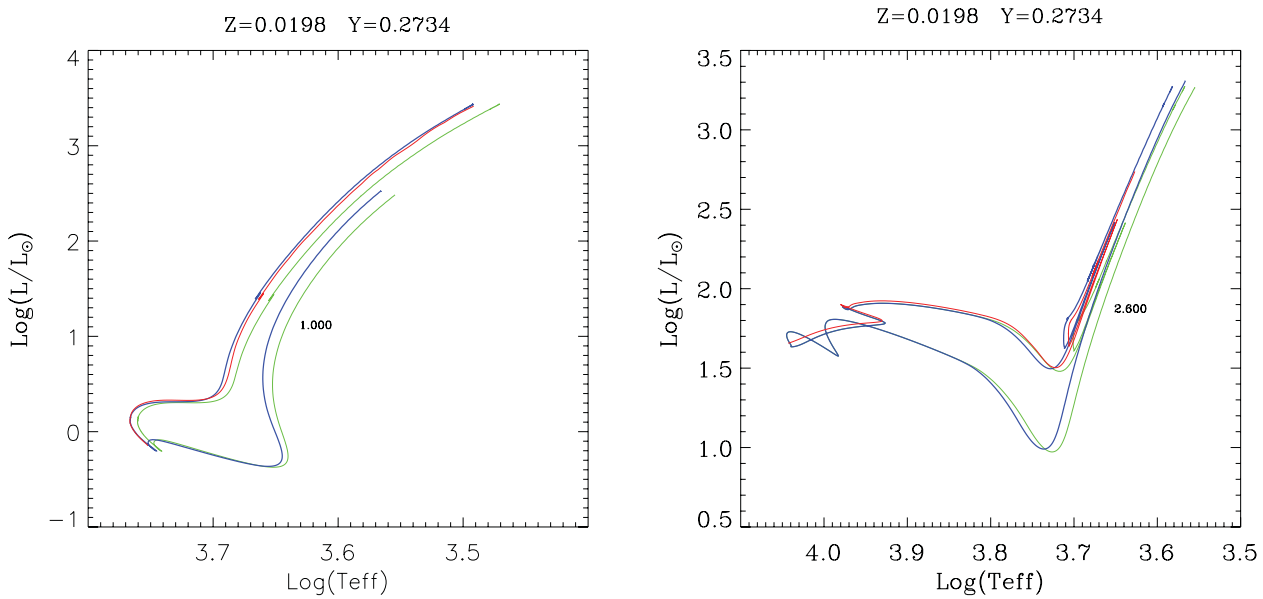

Figure 14. Comparison with BaSTI tracks (Pietrinferni et al. 2004) in the HR diagram. The two panels show tracks for masses of 1.0 and 2.6 $M_{\odot}$ obtained from the BaSTI (red lines) data base for the same fixed solar-scaled abundance of $Z = 0.0198$, $Y = 0.2734$ (based on Grevesse & Sauval 1998) and $\alpha_{MLT} = 1.913$. The blue lines are PARSEC scaled-solar tracks obtained for the same composition and α_{MLT} value as in BaSTI, whereas the green lines are the same but using the PARSEC calibration of the mixing length parameter, i.e. $\alpha_{MLT} = 1.74$.

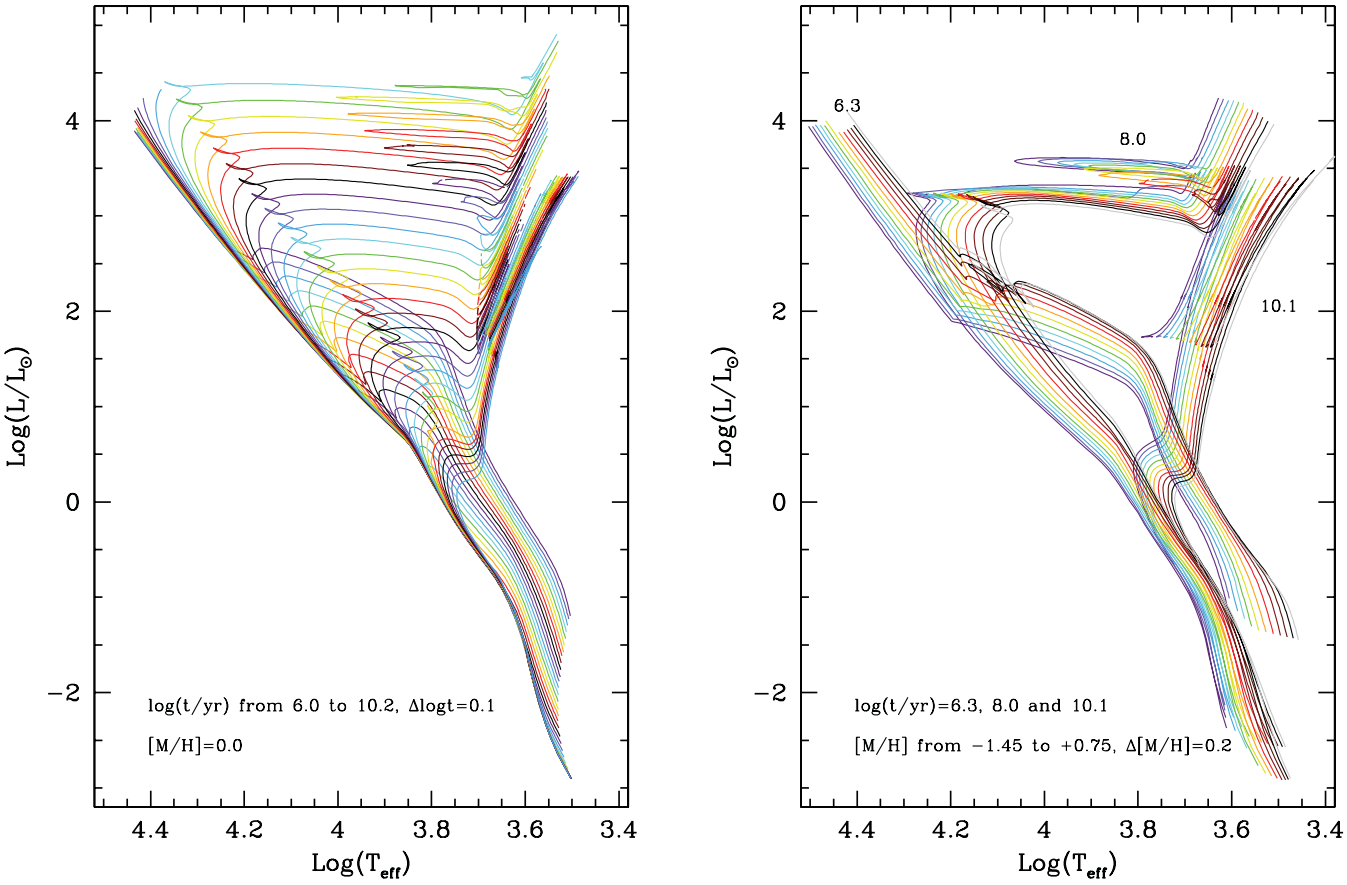

Figure 15. Examples of theoretical isochrones in the HR diagram. Left-hand panel: a sequence of solar-metallicity isochrones for ages going from $\log(t/\mathrm{yr}) = 6$ to 10.2 at equally spaced intervals of $\Delta \log t = 0.1$. Right-hand panel: three sequences of isochrones for a fixed age and at varying metallicities. The ages are $\log(t/\mathrm{yr}) = 6.3$, 8.0 and 10.1. The sequence of metallicities goes from [M/H] = −1.45 to +0.75 at equally spaced intervals of Δ[M/H] = 0.2. In all cases, the mass-loss parameter is assumed to be $\eta = 0.2$, and the sequences are completed down to 0.1 $M_{\odot}$. Note the presence of the PMS phase in the youngest isochrones.

set as $\eta = 0.2$, which is representative of the modest values recently determined by Miglio et al. (2012), based on the asteroseismic data for two star clusters in the *Kepler* fields.

The initial point of each isochrone is the $0.1\,M_{\odot}$ model in the lower main sequence. The terminal stage of the isochrones is either the beginning of the TP-AGB for low- and intermediate-mass stars ($M \leq M_{\rm IM}$, ages $\gtrsim 10^8$ yr) or C ignition for more massive stars.

Theoretical luminosities and effective temperatures along the isochrones are translated into magnitudes and colours using extensive tabulations of bolometric corrections and colours, as detailed in Girardi et al. (2002, 2008), Marigo et al. (2008) and Rubele et al. (2012). The tabulations were obtained from convolving the spectral energy distributions contained in the libraries of stellar spectra of Castelli & Kurucz (2003), Allard et al. (2000, 2001) and Fluks et al. (1994) with the response function of several medium- and broad-band filters. The reference spectrum for Vegamag systems is taken from Bohlin (2007).

The bulk of stars modelled in optical filters, for $T_{\rm eff}$ between 50 000 and ∼4000 K, have their colours based on the Castelli & Kurucz (2003) *ATLAS9* models. Casagrande et al. (2010) have recently and accurately revised the temperature scale of nearby stars via the infrared flux method. It is extremely reassuring to note that, for the Sun, the colour differences between their calibration and Castelli & Kurucz (2003) models are in general only $\simeq$0.02 mag (which is also comparable to the random errors in the calibration; see their table 7), all the way from the *B* to the *H* band.

The isochrones are initially made available through the CMD web interface at OAPD.[8] It allows isochrones to be retrieved for any given choice of age and initial metallicity, within the range of the calculated tracks. Output tables include the most relevant stellar parameters along the isochrones (e.g. L, $T_{\rm eff}$, g, radius, evolutionary phase) and the absolute magnitudes in the photometric system of choice. Isochrones are now provided in more than 30 photometric systems corresponding to major astronomical facilities and surveys. However, the list of photometric systems is being continuously expanded, and updated in response to changes into filter transmission curves and zero-points. We anticipate that the same web interface is being restructured in order to deal with the entire variety of stellar parameters stored in the PARSEC evolutionary tracks.

7 DISCUSSION AND CONCLUDING REMARKS

We have discussed the main features of the new code PARSEC that will be used to update and extend the Padova data base of stellar evolutionary tracks and isochrones. In PARSEC, we have modified and updated all the major input physics, including the EOS, the opacities, the nuclear reaction rates and nuclear network, and the inclusion of microscopic diffusion.

With the new code, we have computed several sets of stellar evolutionary tracks that differ from the previous ones in a few additional aspects. (1) They are based on a new reference solar composition from Caffau et al. (2011). The present code however allows the quick computation of tracks with modified metal distributions (e.g. α enhancement or depletion), fully taking into account the changes implied to tables of opacities and EOS. (2) We consider the evolution along the PMS phase. (3) A few changes have been introduced on the way the convection is treated. From these tracks, we obtain preliminary isochrones up to the beginning of the TP-AGB.

[8] http://stev.oapd.inaf.it/cmd

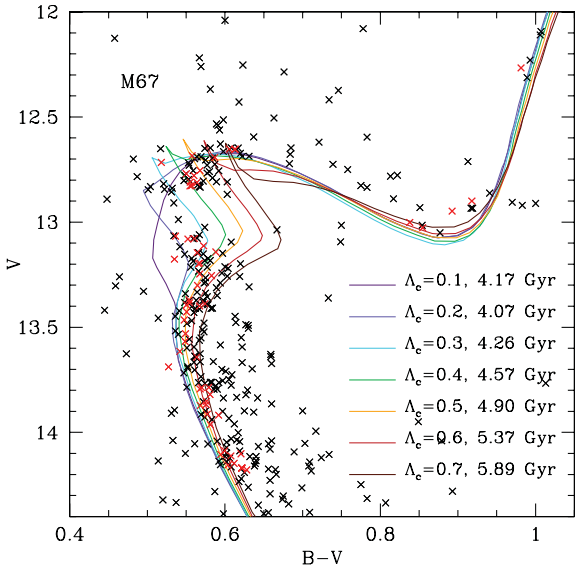

Figure 16. PARSEC isochrones overlaid in the CMD of the intermediate-age star cluster M 67. The distance modulus and colour excess were fixed as $V - M_V = 9.75$ and $E(B - V) = 0.03$, as shown in Fig. 17 next. The *BV* photometry is taken from Montgomery, Marschall & Janes (1993, black points). Red dots mark the 'high-probability single stars' identified by Sandquist (2004). The isochrones are for $Z = 0.014$, and for several values of overshooting parameter Λ_c. The ages are selected so as to reasonably fit the position of the subgiant branch, and especially its lower boundary which coincides with the locus of bona-fide single stars. Note that the isochrones with $\Lambda_c < 0.4$ and $\Lambda_c > 0.6$ fail in reproducing the position and shape of the turnoff region.

Examples of the quality of the new isochrones are shown in Figs 16 and 17 where we present preliminary fits of the colour magnitude diagrams of the Galactic open cluster M 67 and the SMC cluster NGC 419.

M 67 is the best example of an intermediate-age cluster in which the turnoff region presents the clear signatures of well-developed convective cores, in particular the sizeable gap in the concentration of stars at the termination of the main sequence, which is followed by the rapid contraction of the previously convective cores, soon after H exhaustion at the centre. This cluster indicated the need for a quick increase of overshooting efficiency with mass, as advanced in Section 2.6.1. Indeed, Fig. 16 shows a series of isochrones obtained from PARSEC tracks with overshooting parameter going from $\Lambda_c = 0.1$ to 0.7 for the near-solar composition of $Z = 0.014$, $Y = 0.273$ ([M/H] = −0.02). In all cases, the isochrone age was fixed so as to produce about the same description of the subgiant phase, along the line that joins the bona fide single stars located between the reddest termination of the turnoff region and the lower extremity of the first-ascent RGB. The distance and reddening of the isochrones is fixed so as to satisfactorily reproduce the mean position of the RGB, the lower main sequence and the red clump of He-burning stars, as can be appreciated in the left-hand panel of Fig. 17.[9] Therefore, all these isochrones differ mainly in their description of the turnoff region. The figure reveals that isochrones with $\Lambda_c < 0.4$ present a too blue turnoff, compared to the locus of bona fide single stars in M67. Conversely, isochrones with $\Lambda_c > 0.5$ have clearly

[9] We recall that for the typical masses in these isochrones, the red clump position does not vary with the overshooting efficiency, since the core mass at the RGB tip is practically insensitive to this parameter.

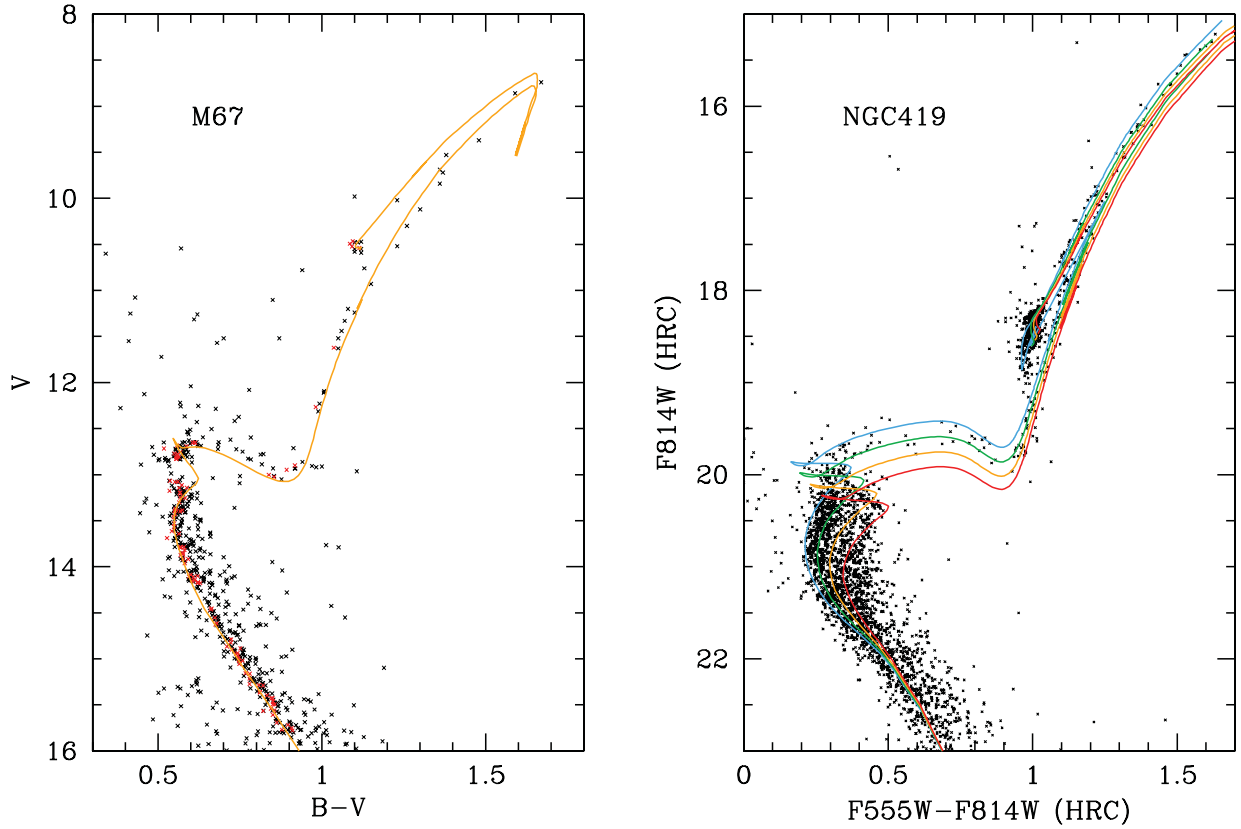

Figure 17. PARSEC isochrones overlaid in the CMDs of two intermediate-age star clusters. In both cases, the distance modulus and reddening were fixed 'by eye' so as to reproduce the position of the red clump. Left-hand panel: the Galactic open cluster M 67. The data are the same as in Fig. 16. The isochrones are for $Z = 0.014$ and $\log(t/\mathrm{yr}) = 9.6$, distance modulus of $V - M_V = 9.75$ and colour excess $E(B - V) = 0.03$. Right-hand panel: the core of the SMC cluster NGC 419. The photometry comes from archival *HST* images obtained with the High Resolution Channel of the Advanced Camera for Surveys onboard the *HST* (GO-10396, PI: J.S. Gallagher), and reduced as described in Girardi et al. (2009). In order to reduce the presence of blends and spurious objects, we plot only those stars with a sharpness of $(\mathrm{sharp}^2_{\mathrm{F555W}} + \mathrm{sharp}^2_{\mathrm{F814W}})^{0.5} < 0.1$. The isochrones are for $Z = 0.004$, ages $\log(t/\mathrm{yr}) = 9.15, 9.20, 9.25, 9.30$ (from blue to red), distance modulus of $\mathrm{F814W} - M_{\mathrm{F814W}} = 18.96$ and colour excess $E_{\mathrm{F555W}-\mathrm{F814W}} = 0.09$.

too red a turnoff. This comparison supports our initial choice for the value of overshooting efficiency for masses $M > M_{02}$, as described in Section 2.6.1. More detailed work is underway, considering the full range of parameters (distances, reddening, metallicity, binary frequency, etc.), as well as the detailed predictions about the occupation probability of different sections of the isochrones.

We also note that M 67 has been the object of many recent analyses aimed at deriving accurate determinations of its age, and constraints on its chemical composition and convective efficiency (see e.g. Michaud et al. 2004; VandenBerg & Stetson 2004; VandenBerg et al. 2007; Magic et al. 2010; Mowlavi et al. 2012). These works were intentionally focused in the turnoff region of the CMD – and especially on its hook-like feature – and did not attempt to fit the RGB and red clump altogether with the same isochrone, as we do in Fig. 17. Our choice of a 'global isochrone fitting' is based on a very simple consideration: our evolutionary tracks are mostly aimed at improving evolutionary population synthesis of resolved and unresolved galaxies for which most observations include very well sampled giant branches. Therefore, a good reproduction of the evolved phases in the CMD is as important in our case, as is the good reproduction of the turnoff region in those more focused works, where the main target is the calibration of physical processes and abundances inside stars.

Another interesting object for a preliminary check of the efficiency of overshooting is the intermediate-age SMC cluster NGC 419. Its CMD (right-hand panel in Fig. 17) presents clear evidences of multiple populations, namely a broad turnoff and a dual red clump (Girardi et al. 2009). The turnoff masses are around the M_{HeF} limit between intermediate- and low-mass stars, as evidenced by the double structure of the red clump. For a cluster of this kind, reproducing the shape of both the turnoff and red clump regions is possible only if the isochrones have about the right amount of overshooting, as discussed in Girardi et al. (2009). As illustrated in Fig. 17, the default PARSEC isochrones (with $\Lambda_c > 0.5$ in the mass range of interest for NGC 419) with ages spanning from 1.4 to 2.0 Gyr are able to reproduce both the 'golf-club' shape of the turnoff region, and the dual structure of the red clump – where the secondary, fainter red clump is explained by the youngest isochrone.

For the moment, our goal is just to call attention to the correct reproduction of the main CMD features, including the shape of the turnoff(s), the subgiant branch, the RGB slope and the red clump(s) in these two clusters. We anticipate that a detailed quantitative analysis of these and other similar clusters is being performed to calibrate the efficiency of overshoot in this mass interval (Rubele et al. in preparation). Younger stellar populations will be considered by Rosenfield et al. (in preparation). The evolution along the TP-AGB, and the corresponding isochrones, will be presented in an accompanying paper (Marigo et al. in preparation).

ACKNOWLEDGMENTS

We thank the anonymous referee for the many suggestions that helped us to improve the final version of this paper, and M. Barbieri, G. Bertelli, A. Miglio and P. Rosenfield for helpful discussions. We acknowledge financial support from contract ASI-INAF I/009/10/0. AB acknowledges financial support from MIUR 2009.

NOTE ADDED IN PROOF

In the published database of stellar models and isochrones, diffusion operates throughout the whole star even in presence of overshoot, until the effects on the evolution of the star become negligible ($M \leq 1.6\ M_{\odot}$). The outermost region, with $M_r/M \geq 0.995$, is always homogenized.

REFERENCES

Allard F., Hauschildt P. H., Alexander D. R., Ferguson J. W., Tamanai A., 2000, in Griffith C. A., Marley M. S., eds, ASP Conf. Ser Vol 212, From Giant Planets to Cool Stars. Astron. Pac. Soc., San Francisco, p. 127
Allard F., Hauschildt P. H., Alexander D. R., Tamanai A., Schweitzer A., 2001, ApJ, 556, 357
Alongi M., Bertelli G., Bressan A., Chiosi C., 1991, A&A, 244, 95
Angulo C. et al., 1999, Nucl. Phys. A, 656, 3
Aparicio A., Bertelli G., Chiosi C., Garcia-Pelayo J. M., 1990, A&A, 240, 262
Asplund M., Grevesse N., Sauval A. J., Scott P., 2009, ARA&A, 47, 481
Bader G., Deuflhard P., 1983, Numerische Matematik, 33, 55
Basu S., Antia H. M., 1997, MNRAS, 287, 189
Basu S., Antia H. M., 2004, ApJ, 606, L85
Basu S., Pinsonneault M. H., Bahcall J. N., 2000, ApJ, 529, 1084
Basu S., Chaplin W. J., Elsworth Y., New R., Serenelli A. M., 2009, ApJ, 699, 1403
Bertelli G., Bressan A., Chiosi C., Fagotto F., Nasi E., 1994, A&AS, 106, 275
Bertelli G., Girardi L., Marigo P., Nasi E., 2008, A&A, 484, 815
Bertelli G., Nasi E., Girardi L., Marigo P., 2009, A&A, 508, 355
Bohlin R. C., 2007, in Sterken C., ed., ASP Conf. Ser. Vol. 364, The Future of Photometric, Spectrophotometric and Polarimetric Standardization. Astron. Pac. Soc., San Francisco, p. 315
Böhm-Vitense E., 1958, Zeitschrift für Astrophysik, 46, 108
Bressan A. G., Chiosi C., Bertelli G., 1981, A&A, 102, 25
Bressan A., Fagotto F., Bertelli G., Chiosi C., 1993, A&AS, 100, 647
Buchmann L., 1996, ApJ, 468, L127
Caffau E., Ludwig H.-G., 2007, A&A, 467, L11
Caffau E., Steffen M., Sbordone L., Ludwig H.-G., Bonifacio P., 2007, A&A, 473, L9
Caffau E., Sbordone L., Ludwig H.-G., Bonifacio P., Steffen M., Behara N. T., 2008, A&A, 483, 591
Caffau E., Ludwig H.-G., Steffen M., Ayres T. R., Bonifacio P., Cayrel R., Freytag B., Plez B., 2008, A&A, 488, 1031
Caffau E., Maiorca E., Bonifacio P., Faraggiana R., Steffen M., Ludwig H.-G., Kamp I., Busso M., 2009, A&A, 498, 877
Caffau E., Ludwig H.-G., Bonifacio P., Faraggiana R., Steffen M., Freytag B., Kamp I., Ayres T. R., 2010, A&A, 514, A92
Caffau E., Ludwig H.-G., Steffen M., Freytag B., Bonifacio P., 2011, Sol. Phys., 268, 255
Casagrande L., Ramírez I., Meléndez J., Bessell M., Asplund M., 2010, A&A, 512, A54
Cassisi S., Marín-Franch A., Salaris M., Aparicio A., Monelli M., Pietrinferni A., 2011, A&A, 527, A59
Castellani V., degl'Innocenti S., 1999, A&A, 344, 97
Castelli F., Kurucz R. L., 2003, in Piskunov N., Weiss W. W., Gray D. F., eds, IAU Symp. Vol. 210, Modelling of Stellar Atmospheres. Astron. Soc. Pac. San Francisco, p. 20
Caughlan G. R., Fowler W. A., 1988, Atomic Data Nucl. Data Tables, 40, 283
Chaboyer B., Fenton W. H., Nelan J. E., Patnaude D. J., Simon F. E., 2001, ApJ, 562, 521
Chafa A. et al., 2007, Phys. Rev. C, 75, 035810
Chiosi C., Bertelli G., Bressan A., 1992, ARA&A, 30, 235
Christensen-Dalsgaard J., Monteiro M. J. P. F. G., Rempel M., Thompson M. J., 2011, MNRAS, 414, 1158
Cyburt R. H. et al., 2010, ApJS, 189, 240
Dababneh S., Heil M., Käppeler F., Görres J., Wiescher M., Reifarth R., Leiste H., 2003, Phys. Rev. C, 68, 025801
De Marchi G., Panagia N., Romaniello M., Sabbi E., Sirianni M., Prada Moroni P. G., Degl'Innocenti S., 2011, ApJ, 740, 11
de Meulenaer P., Carrier F., Miglio A., Bedding T. R., Campante T. L., Eggenberger P., Kjeldsen H., Montalbán J., 2010, A&A, 523, A54
Deheuvels S. et al., 2010, A&A, 514, A31
Dell'Omodarme M., Valle G., Degl'Innocenti S., Prada Moroni P. G., 2012, A&A, 540, A26
Descouvemont P., Adahchour A., Angulo C., Coc A., Vangioni-Flam E., 2004, Atomic Data Nucl. Data Tables, 88, 203
Dewitt H. E., Graboske H. C., Cooper M. S., 1973, ApJ, 181, 439
Di Cecco A. et al., 2010, ApJ, 712, 527
Dotter A., Chaboyer B., Jevremović D., Kostov V., Baron E., Ferguson J. W., 2008, ApJS, 178, 89
Fagotto F., Bressan A., Bertelli G., Chiosi C., 1994, A&AS, 104, 365
Fluks M. A., Plez B., The P. S., de Winter D., Westerlund B. E., Steenman H. C., 1994, A&AS, 105, 311
Fynbo H. O. U. et al., 2005, Nat, 433, 136
Girardi L., Bressan A., Bertelli G., Chiosi C., 2000, A&AS, 141, 371
Girardi L., Bertelli G., Bressan A., Chiosi C., Groenewegen M. A. T., Marigo P., Salasnich B., Weiss A., 2002, A&A, 391, 195
Girardi L., Rubele S., Kerber L., 2009, MNRAS, 394, L74
Girardi L. et al., 2008, PASP, 120, 583
Görres J., Arlandini C., Giesen U., Heil M., Käppeler F., Leiste H., Stech E., Wiescher M., 2000, Phys. Rev. C, 62, 055801
Graboske H. C., Dewitt H. E., Grossman A. S., Cooper M. S., 1973, ApJ, 181, 457
Gratton R. G. et al., 2001, A&A, 369, 87
Grevesse N., Sauval A. J., 1998, Space Sci. Rev., 85, 161
Guenther D. B., Demarque P., Kim Y.-C., Pinsonneault M. H., 1992, ApJ, 387, 372
Haft M., Raffelt G., Weiss A., 1994, ApJ, 425, 222
Hale S. E., Champagne A. E., Iliadis C., Hansper V. Y., Powell D. C., Blackmon J. C., 2002, Phys. Rev. C, 65, 015801
Hale S. E., Champagne A. E., Iliadis C., Hansper V. Y., Powell D. C., Blackmon J. C., 2004, Phys. Rev. C, 70, 045802
Iglesias C. A., Rogers F. J., 1996, ApJ, 464, 943
Iliadis C., D'Auria J. M., Starrfield S., Thompson W. J., Wiescher M., 2001, ApJS, 134, 151
Imbriani G. et al., 2005, Eur. Phys. J. A, 25, 455
Itoh N., Kohyama Y., 1983, ApJ, 275, 858
Itoh N., Uchida S., Sakamoto Y., Kohyama Y., Nozawa S., 2008, ApJ, 677, 495
Kamath D., Wood P. R., Soszyński I., Lebzelter T., 2010, MNRAS, 408, 522
Kippenhahn R., Weigert A., Hofmeister E., 1967, J. R. Astron. Soc. Can., 61, 387
Komatsu E. et al., 2011, ApJS, 192, 18
Lodders K., Palme H., Gail H.-P., 2009, in Trümper J. E., ed., Landolt-Börnstein – Group VI Astronomy and Astrophysics Numerical Data and Functional Relationships in Science and Technology. Volume 4B: Solar system. Springer, Berlin, p. 44
Magic Z., Serenelli A., Weiss A., Chaboyer B., 2010, ApJ, 718, 1378
Marigo P., Aringer B., 2009, A&A, 508, 1539
Marigo P., Girardi L., 2007, A&A, 469, 239
Marigo P., Girardi L., Chiosi C., Wood P. R., 2001, A&A, 371, 152
Marigo P., Girardi L., Bressan A., Groenewegen M. A. T., Silva L., Granato G. L., 2008, A&A, 482, 883

Meléndez J., Casagrande L., Ramírez I., Asplund M., Schuster W. J., 2010, A&A, 515, L3
Meynet G., Maeder A., Schaller G., Schaerer D., Charbonnel C., 1994, A&AS, 103, 97
Michaud G., Richard O., Richer J., VandenBerg D. A., 2004, ApJ, 606, 452
Miglio A. et al., 2012, MNRAS, 419, 2077
Molaro P., Bressan A., Barbieri M., Marigo P., Zaggia S., 2012, Mem. Soc. Astron. Ital. Suppl., 22, 233
Montgomery K. A., Marschall L. A., Janes K. A., 1993, AJ, 106, 181
Mowlavi N., Eggenberger P., Meynet G., Ekström S., Georgy C., Maeder A., Charbonnel C., Eyer L., 2012, A&A, 541, A41
Mucciarelli A., Caffau E., Freytag B., Ludwig H.-G., Bonifacio P., 2008, A&A, 484, 841
Munakata H., Kohyama Y., Itoh N., 1985, ApJ, 296, 197
Nordlander T., Korn A. J., Richard O., Lind K., 2012, ApJ, 753, 48
Pietrinferni A., Cassisi S., Salaris M., Castelli F., 2004, ApJ, 612, 168
Reimers D., 1975, Mem. Soc. R. Sci. Liege, 8, 369
Richer J., Michaud G., Turcotte S., 2000, ApJ, 529, 338
Rubele S. et al., 2012, A&A, 537, A106
Salasnich B., 1999, PhD thesis, University of Padova
Sandquist E. L., 2004, MNRAS, 347, 101
Serenelli A. M., Basu S., Ferguson J. W., Asplund M., 2009, ApJ, 705, L123
Thoul A. A., Bahcall J. N., Loeb A., 1994, ApJ, 421, 828
Turcotte S., Richer J., Michaud G., Iglesias C. A., Rogers F. J., 1998, ApJ, 504, 539
VandenBerg D. A., Stetson P. B., 2004, PASP, 116, 997
VandenBerg D. A., Gustafsson B., Edvardsson B., Eriksson K., Ferguson J., 2007, ApJ, 666, L105
VandenBerg D. A., Bergbusch P. A., Dotter A., Ferguson J. W., Michaud G., Richer J., Proffitt C. R., 2012, ApJ, 755, 15
Vauclair S., 1983, in Cox A. N., Vauclair S., Zahn J. P., eds, Saas-Fee Advanced Course 13, Astrophysical Processes in Upper Main Sequence Stars. Geneva Observatory, Geneva, p. 167
Wilmes S., Wilmes V., Staudt G., Mohr P., Hammer J. W., 2002, Phys. Rev. C, 66, 065802

This paper has been typeset from a TEX/LATEX file prepared by the author.